

## 9. SITE 979<sup>1</sup>

### Shipboard Scientific Party<sup>2</sup>

#### HOLE 979A

**Date occupied:** 0745, 21 June 1995

**Date departed:** 0715, 25 June 1995

**Time on hole:** 3 days, 23 hr, 30 min

**Position:** 35°43.427'N, 3°12.353'W

**Drill pipe measurement from rig floor to seafloor (m):** 1074.0

**Distance between rig floor and sea level (m):** 11.9

**Water depth (drill pipe measurement from sea level, m):** 1062.1

**Total depth (from rig floor, m):** 1654.9

**Penetration (m):** 580.9

**Number of cores (including cores having no recovery):** 62

**Total length of cored section (m):** 580.9

**Total core recovered (m):** 583.14

**Core recovery (%):** 100.4

**Oldest sediment cored:**

Depth (mbsf): 580.9

Nature: Claystone

Age: late Pliocene

**Principal results:** Site 979 is located in the Southern Alboran Basin, a narrow depression between Alboran Island and the Moroccan coast, about 45 km north of Cabo Tres Forcas (Morocco). The site is situated south of the northeast-southwest-trending Alboran Ridge. The ridge is more than 30 km wide, ~150 km long, rises ~1000 m above the surrounding basin floor, and rises above sea level at Alborán Island. Site 979 was chosen in an area where seismic data indicated a zone of syn- and postsedimentary deformation, including Pleistocene–Holocene deformation and tilting. The deformation is expressed as a series of folds and faults that extend from the southern flank of the Alboran Ridge to the adjacent basin floor. Our main objectives were to determine the age and stratigraphy of the uppermost part of the basin fill and to constrain the age of the deformation, which is thought to represent later stages of compressional reorganization of the Alboran Basin.

Site 979 was drilled to a total depth of 580.9 mbsf. At that point, we had to stop drilling to allow time for logging operations before the end of the leg. After excellent recovery and core quality in the upper part of the section, APC coring was terminated at 134.5 mbsf. Recovery in the XCB-cored interval was high, but the cores were extensively biscuited. Unfortunately, the biscuiting destroyed a significant portion of the original sediment texture, severely limiting sedimentological and structural observations to short (<10 cm) pieces of cores. In addition, recovered cores were highly gassy, which also caused considerable disturbance.

The stratigraphic interval recovered ranges from upper Pliocene (Subzone NN16A, MPL 5a) to uppermost Pleistocene/Holocene (NN21B, *G. truncatulinoides excelsa* Zone). The Pliocene/Pleistocene boundary is ap-

proximated by the NN19B/NN19A subzonal boundary (between 340.77 and 345.33 mbsf). Calcareous nannofossils and planktonic foraminifers are abundant and well preserved in most of the sequence. Zone MPL5a (upper Pliocene) is consistently present down to 569.78 mbsf, and Zone MPL4b was not reached. Benthic foraminifers suggest lower epibathyal (500–1300 m) to upper mesobathyal (1000–1800 m) depths for these sediments. Average sedimentation rates at Site 979 were 200 m/m.y. for the Pleistocene and 184–191 m/m.y. for the upper Pliocene. A short hiatus within the upper Pliocene was recognized. The biostratigraphic age data suggest an increase in the sedimentation rate to 696 m/m.y.

The sediments recovered at Site 979 were quite uniform and only one lithological unit is recognized, which covers the entire interval from 0 to 580.9 mbsf. The sediments consist of Pleistocene to Pliocene open-marine hemipelagic deposits with minor siliciclastic detrital layers. The dominant lithology is gray to green nannofossil clay, which accounts for about 40% of the stratigraphic section. A typical composition of these hemipelagic facies is about 53% clay, 40% calcareous nannofossils, 6% micrite, 1% foraminifers, and trace amounts of detrital mica, opaque minerals, sponge spicules, and fecal pellets. Shell fragments and dispersed silt-sized foraminifers are variably present. Disseminated grains, clusters, and very rare nodules of pyrite are found throughout the unit, as are trace amounts of glauconite. Bioturbation is common but varies in intensity throughout the entire sequence and includes *Chondrites*, *Planolites*, and *Zoophycos*. Minor lithologies include diatom- and organic-rich silty-clay layers, discrete sandy and silty layers, and intraformational breccia. Silty and sandy turbidites occur throughout the sequence. The unconformity identified from biostratigraphic data that lies between 475.35 and 477.46 mbsf is marked by a weakly bioturbated to structureless nannofossil-rich clay with no obvious breaks in the sedimentary record.

The Pliocene to Pleistocene sediments recovered at Site 979 are for the most part horizontal, but there are local intervals of dipping beds that may have resulted from slump folding. Some intervals show a variably developed and variably oriented fissility oblique to the bedding, and, in addition, they show fractures parallel to the core. The fissility appears to be an incipient disjunctive cleavage, and it may be a response to deformation associated with the nearby Alboran Ridge.

The interstitial water profiles at Site 979 appear to be influenced by two main processes: early diagenesis of organic matter and the presence of a saline brine at depth. There are downhole linear increases in calcium, salinity, chlorine, sodium, and lithium, which suggest a deep supply for these elements. Alkalinity peaks at 16 mM at 24.96 mbsf, and decreases below this depth to below seawater values at total depth. Strontium concentrations increase from seawater concentrations at the top of the cored sequence to 3 mM at total depth, which is >30 times higher than seawater concentrations. Sulfate decreases from seawater concentrations to zero at 24.95 mbsf, which reflects bacterial degradation of organic matter through sulfate reduction.

Heat flow at Site 979 is 79 mW/m<sup>2</sup>, which is significantly less than that reported at other sites in this area. Calculating heat flow using the shallowest measurement at 20.5 mbsf and its delta temperature (in situ minus mudline) of 2.04°C, the result is 111 mW/m<sup>2</sup>, close to the 118 ± 8 mW/m<sup>2</sup> reported from nearby sites. This suggests that there may have been a recent change in bottom-water temperature.

Concentrations of carbonate carbon vary up to 8.3% and are equivalent to 2% to 69% sedimentary CaCO<sub>3</sub>. Total organic carbon concentrations (TOC) reach up to 2.0%. Average TOC concentration is 0.7%, which

<sup>1</sup>Comas, M.C., Zahn, R., Klaus, A., et al., 1996. *Proc. ODP, Init. Repts.*, 161: College Station, TX (Ocean Drilling Program).

<sup>2</sup>Shipboard Scientific Party is given in the list preceding the Table of Contents.

is more than twice the deep-sea average of 0.3%. The elevated TOC concentrations of these sediments are probably a consequence of high sedimentation rates, which improve organic matter preservation. Organic matter C/N ratios reach as high as 20, but most are between 4 and 8, which is representative of algal organic matter. Rock-Eval analysis indicates that some marine organic matter has been oxidized, probably by microbial reworking.

Elevated amounts of headspace gas, including higher molecular-weight thermogenic gases, were encountered. High  $C_1/C_2$  ratios indicate that the methane is biogenic in origin. Concentrations of propane exceed those of ethane in sediments below about 300 mbsf and exceed 100 ppm at the bottom of Hole 979A, suggesting that propane was produced by thermal degradation of sedimentary organic matter during some former period of elevated heat flow in the Southern Alboran Basin.

Remanent magnetic directions seem to be extensively overprinted at Site 979. The overprint is almost antiparallel to the radial remagnetization observed at the other Leg 161 sites (974, 975, 976, 977, and 978) and points to an acquisition of anhysteretic remanent magnetization. Due to this overprint, magnetostratigraphic polarity zones could not be identified at Site 979.

Physical property data indicate smooth variation in properties down-hole. GRAPE data show several distinct changes in slope, which may be related to subtle changes in sediment strength. Velocity measurements were hampered by the gassy nature of the cores.

Quad combo log data were acquired from 60 to 277 mbsf. The entire logged section appears to be rather homogeneous as is reflected in the recovered cores. Between 157 and 168 mbsf, however, intervals with abrupt decreases in resistivity and acoustic velocity are found.

Site 979 results will allow us to constrain the age of the deformation in the Southern Alboran Basin and around the Alboran Ridge. Comparing seismic data and drilling results suggests that tectonic activity, including uplifting by folding and/or faulting of the Alboran Ridge, occurred from the upper Pliocene to the Holocene. The high sedimentation rates suggest that active subsidence and sedimentation was concomitant with uplifting in surrounding areas. No volcanic or volcanoclastic material was found at Site 979, indicating no volcanic activity during upper Pliocene to Pleistocene times. This implies that the volcanic Alboran Ridge was not active during these times. Although we terminated coring about 40 m before reaching a major angular-unconformity visible on seismic profiles, extrapolation of our data indicates that the unconformity may correspond to the same erosional unconformity that was cored at Sites 977 and 978 and likely corresponds to the "M"-reflector in the Southern Alboran Basin.

## BACKGROUND AND OBJECTIVES

Site 979 is located in the Southern Alboran Basin (SAB), a narrow depression between the Alborán Island and the Moroccan coast, about 45 km north of Cabo Tres Forcas. The site is situated at the base of the southern flank of the northeast-southwest-trending Alboran Ridge, a main topographic feature of the Alboran Sea. Site survey seabeam bathymetry (ALBA Cruise, 1992) indicates that the ridge is more than 30 km wide, ~150 km long, and rises ~1000 m above the surrounding basin floor. It has a highly irregular physiography with numerous steep pinnacles and deep gullies. The ridge emerges above sea level at Alborán Island, which is formed of volcanic rocks (Hernandez et al., 1987). The ridge continues below sea level to the west along the Xauen Bank, which extends toward the Western Alboran Basin (WAB; Fig. 1).

Site 979 was drilled at shotpoint 520 of multichannel seismic reflection line RAY-36, where seismic data indicate a zone of syn- and postsedimentary deformation (Figs. 2, 3). The deformation is expressed as a series of folds and faults on the flanks of the ridge. On the southern flank, seismic data indicate that the deformed zone is 5 km wide and extends laterally for up to 50 km. Deformation and tilting appear to be Pleistocene-Holocene in age (Fig. 4). The southern flank of the ridge aligns with the Jebha Fault in Morocco (see Fig. 4 of "Background and Objectives" section, "Site 977" chapter, this volume) and, therefore, may form part of a major sinistral strike-slip fault system across the Alboran Sea (see "Introduction" chapter, this volume).

Our primary drilling objective at Site 979 was to penetrate and sample two main unconformities, which lie at 0.22 s TWT (~230 mbsf) and 0.63 s TWT (~620 mbsf) in seismic line RAY-36, respectively (Fig. 3). Seismic data indicate that the lower unconformity should correspond to the "M"-reflector, which, in most of the Alboran Sea region, corresponds to an erosional surface, and, in the Southern Alboran Basin, is deformed by compressional tectonics (Comas et al., 1992).

The sedimentary cover in the SAB has a maximum thickness of 4 s (4.5 km) and overlies northeast-southwest-trending basement highs (Fig. 3), some of which may be of volcanic origin (Giermann et al., 1968). The stratigraphy of the sediments filling this basin is not well known, but seismic data suggest that it may be early Miocene to Pleistocene in age. Data from the El Jebha-1 well on the Xauen Bank, the westernmost extension of the basin, indicate that a thin blanket of

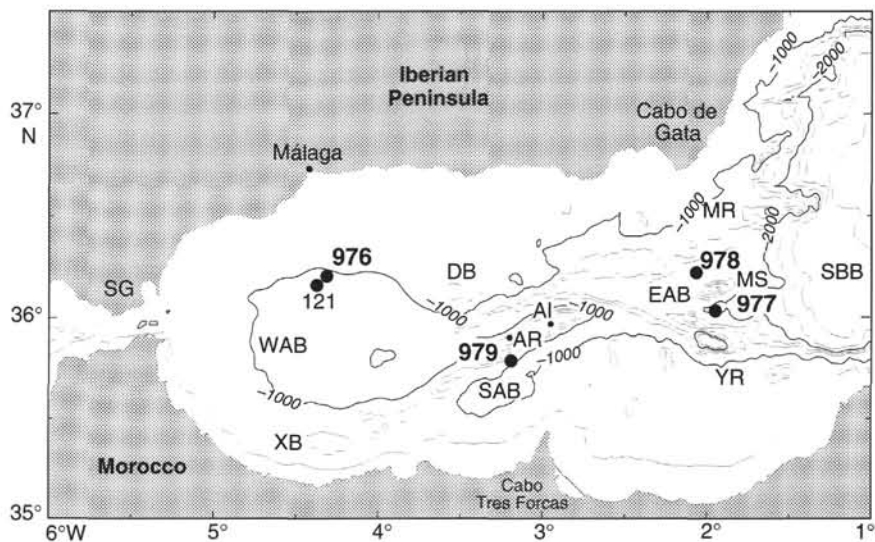


Figure 1. Location of Leg 161 Sites 976, 977, 978, 979, and DSDP Site 121 in the Alboran Sea. Contours in meters, contour interval is 200 m. AI = Alborán Island, AR = Alboran Ridge, DB = Djibuti Bank, EAB = Eastern Alboran Basin, MR = Maimonides Ridge, MS = Al-Mansour Seamount, SAB = Southern Alboran Basin, SBB = Southern Balearic Basin, SG = Strait of Gibraltar, WAB = Western Alboran Basin, XB = Xauen Bank, YR = Yusuf Ridge.

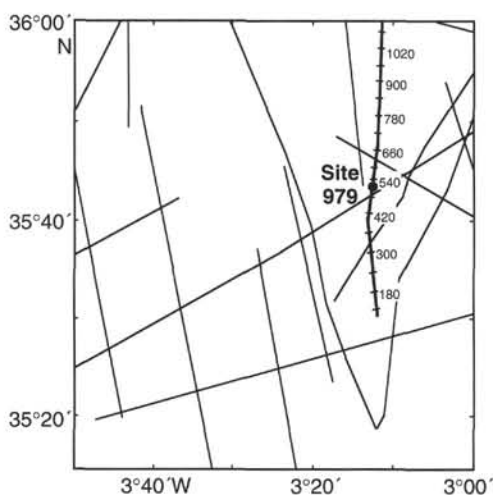


Figure 2. Location of multichannel seismic reflection lines around Site 979. Shotpoints of seismic profile in Figure 3 are shown.

Pliocene–Pleistocene sediments overlies a thick late- to mid-Miocene sequence (Bourgeois et al., 1992).

The Alboran Ridge is considered to be a fault-bounded, uplifted, structural high. Seismic data suggest that there was tectonic activity from the late Miocene to the Pleistocene. Major structures with similar northeast-southwest-trending directions outcrop in southeast Spain (e.g., Carboneras Fault) and have been attributed to left-lateral transcurrent tectonics (De Larouzière et al., 1988). From the existing seismic data, however, it is not clear if the Alboran Ridge is an anticlinal structure (Bourgeois et al., 1992), a major sinistral strike-slip fault (the “trans-Alboran shear zone” of De Larouzière et al., 1988), or an uplifted horst bounded by transtensive or transpressive faults (Comas et al., 1992; Woodside and Maldonado, 1992; Watts et al., 1993). The acoustic basement of the southern flank of the Alboran Ridge (Fig. 5), sampled during a 1994 submersible dive (CY-ANALBORAN Cruise), recovered dacitic and rhyodacitic volcanic rocks (Comas et al., in press).

Specific objectives at Site 979 were to determine:

1. The stratigraphy of the SAB sediment fill, sedimentary environment, and paleogeography. We also intended to correlate sediments cored at Site 979 with the sedimentary sequence at Sites 977 and 978 in the Eastern Alboran Basin.
2. The subsidence/uplifting history of the SAB. Timing of angular unconformities, combined with subsidence analysis, will provide information to understand basin evolution, specifically if the basin evolved from extensional tectonics and later experienced compression.
3. The extent of deformation of the basin and to calibrate basin stratigraphy with time of the later tilting and uplift of the Alboran Ridge and the associated folds and strike-slip faulting. Comparison between recent folding and strike-slip faulting on land and offshore deformation, which occurred contemporaneously with the Pliocene-to-Holocene subsidence of the basin, will allow us to define the later stages of contractional reorganization of the basin.
4. The character of Atlantic-Mediterranean water exchange from the Miocene to the Pleistocene, similar to objectives addressed at other Leg 161 sites in the Alboran Sea (see “Background and Objectives,” section, “Site 977” chapter, this volume).
5. Hydrographic and biogeochemical gradients within the Alboran Sea, especially during times of sapropel formation. In ad-

dition, the combined paleoceanographic database from Sites 977, 978, and 979 will be used to determine productivity patterns and hydrographic variability in the eastern and southern Alboran Sea.

## OPERATIONS

### Transit Site 978 to Site 979 (Alb-3C)

The original Alb-3A site was situated <0.5 nmi from the reported location of a telecommunications cable and drilling there was not allowed. Before arriving on site we received permission to offset and drill about 0.75 nm north of the cable at Site 979 (Alb-3C). After the 63-nmi transit to Site 979 (5.5 hr; 11.45 nmi/hr), we deployed two beacons at 0745 hr and 0945 hr, 21 June. Hole 979A was located at 35°43.427'N, 3°12.353'W. The elevation of the DES above sea level was 11.90 m for Hole 979A.

### Hole 979A

We used the same APC/XCB BHA as was run at all other APC/XCB sites during this leg. We spudded Hole 979A at 1730 hr, 21 June. Core 1H was taken with the bit at 1066.0 mbrf and recovered 1.46 m. The seafloor, therefore, was defined to be at 1062.1 mbsf. Cores 979A-1H to 15H were taken to 134.5 mbsf and recovered 140.42 m (104.42%; Table 1; see also the detailed coring summary on the CD-ROM, back pocket, this volume). Cores were oriented from Core 3H, and ADARA temperature measurements were taken during Cores 3H, 6H, and 9H.

Cores 11H, 14H, and 15H were partial strokes, and we terminated APC-coring after Core 15H. The cores contained significant amounts of gas, and, to minimize gas expansion, small holes were drilled into the liners before cutting them into sections. All of the cores expanded against the inside wall of the APC core barrel, making visible contact-ring marks on the lower part of the liner once it was extruded. Cores 11H, 14H, and 15H, which were partial strokes, became stuck in the inner core barrel and had to be pulled out with a winch.

XCB Cores 16X to 62X were taken from 138.3 to 580.9 mbsf (1208.5 to 1654.9 mbrf) and recovered 442.69 m (99.17%). Despite the expansive nature of the sediment, XCB recovery was very good, although the cores were quite biscuited. Coring parameters were 10,000–25,000 lb WOB and 50 to 70 rpm, with circulation rates of 30 to 45 spm at 200 to 500 psi. The hole was terminated because there was insufficient time remaining to penetrate to 600 mbsf and also log the hole. Overall APC/XCB recovery for Hole 979A was 100.4%.

The maximum methane gas detected in the APC cores was 29,757 ppm (Core 979A-7H) and high methane concentrations near the seafloor were from biogenic processes and did not present any safety problems. The maximum concentration of hydrocarbons from the headspace analysis occurred in Core 979A-31X, where the following contents were reported (in ppm): C<sub>1</sub>: 37,130; C<sub>2</sub>: 17; C<sub>3</sub>: 13. C<sub>1</sub>/C<sub>2</sub> ratios remained relatively constant with depth below Core 979A-26X, ranging between 700 to 1000.

We conditioned the hole for logging with a wiper trip to 79 mbsf (1153 mbrf). Three tight sections of hole were observed at 447, 494, and 528 mbsf (1516, 1568, and 1602 mbrf), and no fill was encountered in the bottom of the hole. The pipe was pulled back to 79 mbsf for logging. The quad combo log was run into the hole but met a bridge at 246 mbsf (1320 mbrf). We decided to log this part of the hole before moving the pipe down to attempt logging deeper in the hole. The caliper data in the APC and XCB portions of the hole were quite different, with the APC section being much more in gauge than the XCB section. This result was also seen in Hole 977A.

After the upper portion of the hole was logged with the quad combo, we removed the tool from the hole and lowered the pipe to 277 mbsf (1351 mbrf). When the tool was run back into the hole it en-

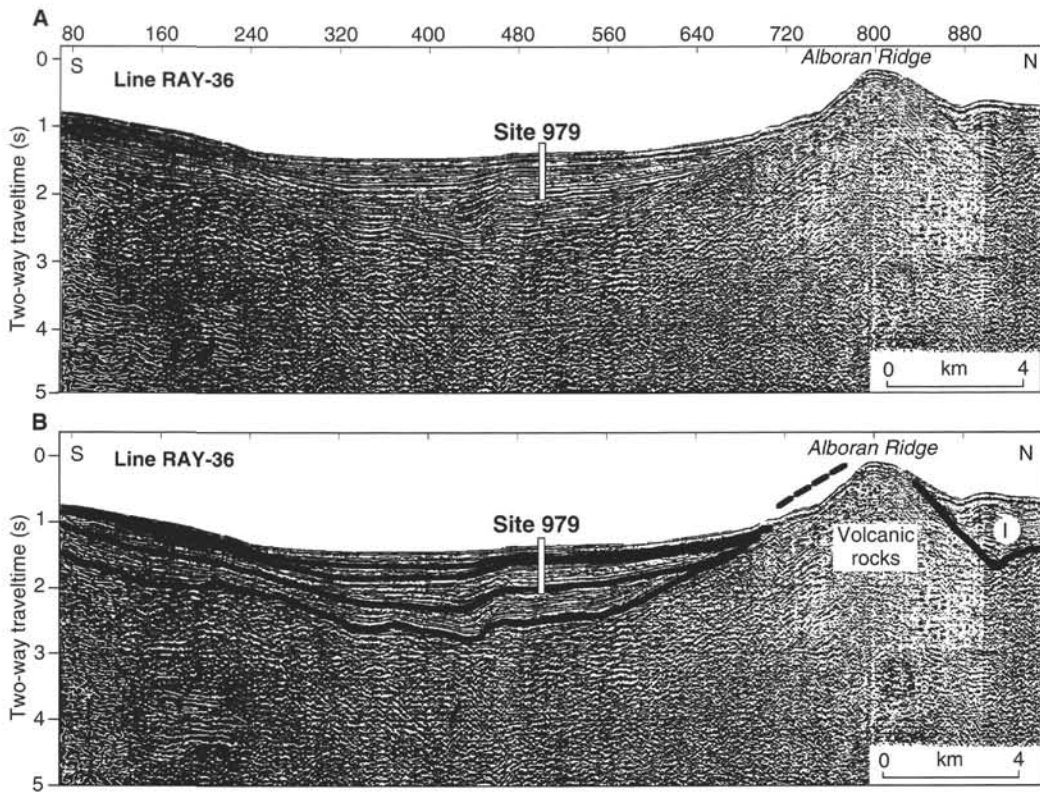


Figure 3. Location of Site 979 on stack MCS profile RAY-36. **A.** Original seismic reflection profile. **B.** Interpreted profile based on seismic sequence analysis and stratigraphic subdivision proposed by Comas et al. (1992). Location of line shown is in Figure 2. Dashed line on the southern side of the Alboran Ridge shows location of *Cyana-4* submersible sampling.

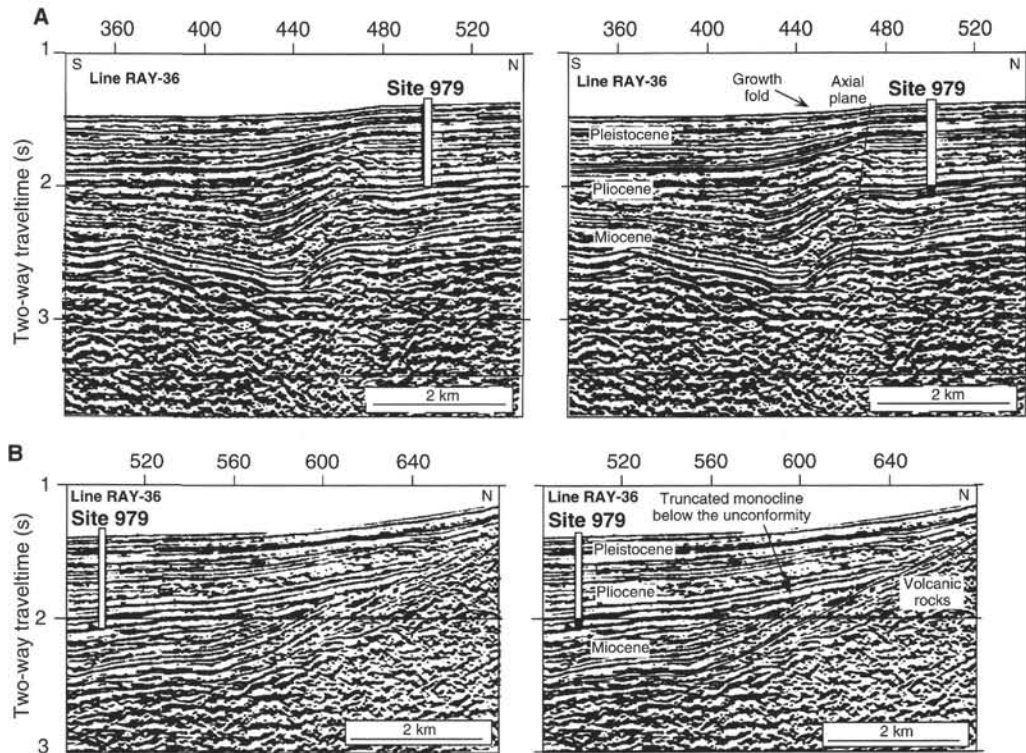


Figure 4. Details of the seismic section RAY-36. **A.** The seafloor is deformed along a fault-propagation fold that controlled the thickness of the Pliocene and Pleistocene sequences. The dip of the deep fault is unclear, but it is interpreted on the basis of the anticline axial plane. **B.** The major truncation visible below the lower Pliocene unconformity is located in the southern flank of the Alboran Ridge. The monocline is about 2.5 km long, rapidly losing dip to the south, beneath Site 979. The monocline has been eroded, probably during the Messinian low-stand. Later tilting of the cover is also visible on the overlying Pliocene–Pleistocene sequences.

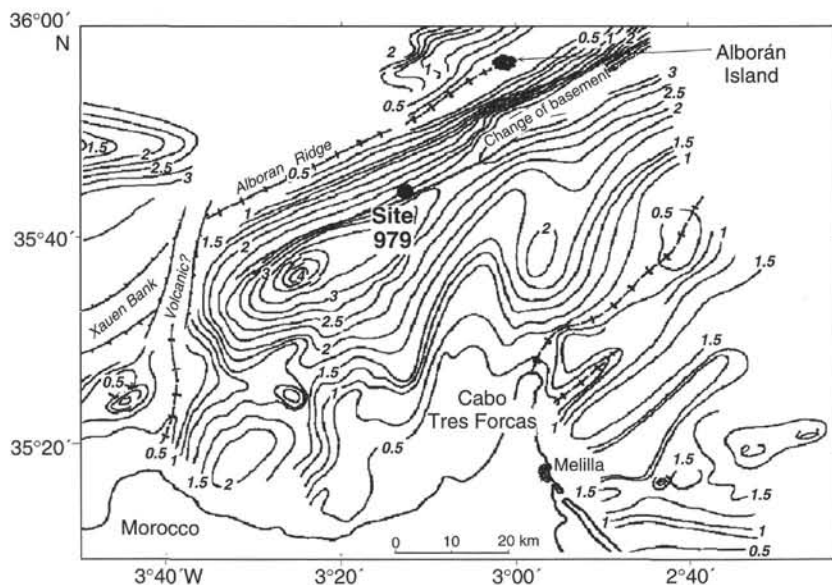


Figure 5. Contour map of basement depth around Site 979. Bathymetric contours in meters. Basement depth contours in seconds TWT. Axes of basement highs and suspected changes in basement lithology, from volcanic in the Alboran Ridge to metamorphic toward the south, are shown. Multi-channel seismic data used to construct this map are shown in Figure 2.

countered numerous tight sections and had to be worked down the hole to 464 mbsf (1538 mbrf) until no further advance could be made. We then logged from 464 to 251 mbsf (1325 mbrf). Caliper data indicated that the hole was moderately washed-out with few continuous sections of hole in gauge. After completing the quad combo logs, there was not enough time remaining to attempt the FMS log or move the pipe lower to log the lowermost 100 m of hole. Logging was completed and the tools rigged down by 2400 hr on 24 June.

The pipe was raised to 79 mbsf (1153 mbrf) and 63 bbl (200 sacks) of cement were pumped into the hole prior to abandoning the hole. The bit cleared the seafloor at 0200 hr on 25 June. We circulated seawater through the pipe to clean any remaining cement residue before tripping back to the ship. While tripping out of the hole, the inner diameter of the pipe was coated with rust-inhibitor.

The bit cleared the rig floor at 0600 hr, 25 June. The back-up beacon was recovered (0230 hr, 25 June) while the drill string was being retrieved. The primary beacon would not release despite our having installed and tested a new release mechanism immediately before deploying the beacon at this site. The ship was secured for transit and departed at 0715 hr for a rendezvous with the *RESE* approximately 20 nmi off of Málaga, Spain. The transfer occurred at approximately 1400 hr, 25 June.

### Sea Voyage to Leith

After making the rendezvous off Málaga, the vessel began the sea voyage to Leith and made for the Strait of Gibraltar. The ~1831 nmi transit from Site 979 to Leith required 179.25 hr (avg. = 10.42 nmi/hr). Because of low tides, the vessel had to meet the harbor pilot at ~1530 hr 2 July and entered the harbor at 1700 hr. Leg 161 ended with the first line ashore in Leith, Scotland, at 1730 hr on 2 July.

### LITHOSTRATIGRAPHY

Site 979 is located on the southern flank of the Alboran Ridge north of the Southern Alboran Basin depocenter (Fig. 1). A single continuously-cored APC/XCB hole (Hole 979A) was drilled to a depth of 580.9 mbsf. The stratigraphic section shows little variation and only one lithostratigraphic unit has been recognized (Fig. 6).

### Unit I: Pleistocene to Pliocene

Hole 979A, 0.0–580.9 mbsf, Section 979A-1H-1, 0 cm, to Section 979A-62X-CC, 32 cm

Unit I comprises 581 m of dominantly open-marine hemipelagic deposits with minor discrete sand and silt layers. The main lithology within Unit I is nannofossil clay, which accounts for about 40% of the stratigraphic section. A typical composition is 53% clay, 40% calcareous nannofossils, 6% micrite, 1% foraminifers, and trace amounts of detrital mica, opaque minerals, sponge spicules and fecal pellets (smear slide 979A-8H-5, 79–80 cm). Other major lithologies are nannofossil silty clay, nannofossil-rich clay, calcareous clay, and calcareous silty clay, each of which compose about 10% of the stratigraphic section. The proportion of clay-sized particles in these major lithologies ranges between 50% and 95% (average 80%), with silt and sand making up 2%–35% (average 17%) and 0%–15% (average 3%), respectively (Fig. 6). Carbonate content of Unit I, as determined by chemical analysis (Fig. 6; see also “Organic Geochemistry” section, this chapter), ranges between 17% and 54% (average 32%). The carbonate fraction of the major lithologies is dominated by nannofossils which range from 3% to 45% (visual estimation from smear slides), but includes foraminifers (0%–5%), bioclasts (0%–10%), and micrite (0%–15%).

Shell fragments are variably present below Section 979A-4H to the bottom of the hole. Abundances range from common to very rare with no clear pattern to the distribution. Dispersed silt-sized foraminifers were first noted in Core 979A-5H and are irregularly present to the base of the hole. Disseminated grains, clusters, and very rare nodules of pyrite and trace amounts of glauconite are present throughout the hole.

Color of the major lithologies varies between gray and green (Fig. 7). The many different shades (dusky yellow green [5GY 5/2], medium greenish gray [5GY 5/1], grayish olive [10Y 4/2], olive gray [5Y 4/1], dark greenish gray [5GY 4/1], medium olive gray [5Y 5/1], and greenish gray [5Y 6/1]) do not correlate with carbonate content.

Bioturbation is common throughout the main lithologies of Unit I, varying in intensity between slight and intense. The most heavily bioturbated lithologies tend to be the darker (grayish olive, 10Y 4/2) nannofossil clays, but this is not ubiquitous. Evidence for bioturba-

Table 1. Site 979 coring summary.

Core	Date (June 1995)	Time (UTC)	Depth (mbsf)	Length cored (m)	Length recovered (m)	Recovery (%)
161-979A-						
1H	21	0905	0.0-1.5	1.5	1.46	97.3
2H	21	0930	1.5-11.0	9.5	10.01	105.3
3H	21	1020	11.0-20.5	9.5	9.84	103.0
4H	21	1110	20.5-30.0	9.5	10.02	105.5
5H	21	1140	30.0-39.5	9.5	9.87	104.0
6H	21	1240	39.5-49.0	9.5	10.10	106.3
7H	21	1320	49.0-58.5	9.5	10.02	105.5
8H	21	1405	58.5-68.0	9.5	10.13	106.6
9H	21	1515	68.0-77.5	9.5	10.41	109.6
10H	21	1600	77.5-87.0	9.5	10.13	106.6
11H	21	1645	87.0-96.5	9.5	6.62	69.7
12H	21	1800	96.5-106.0	9.5	10.58	111.3
13H	21	1830	106.0-115.5	9.5	10.51	110.6
14H	21	1855	115.5-125.0	9.5	10.36	109.0
15H	21	1945	125.0-134.5	9.5	10.39	109.3
16X	21	2035	134.5-138.3	3.8	5.64	148.0
17X	21	2120	138.3-147.9	9.6	9.03	94.0
18X	21	2200	147.9-157.5	9.6	9.10	94.8
19X	21	2245	157.5-167.1	9.6	9.61	100.0
20X	21	2315	167.1-176.8	9.7	9.07	93.5
21X	22	0000	176.8-186.5	9.7	7.97	82.1
22X	22	0040	186.5-196.1	9.6	9.30	96.9
23X	22	0115	196.1-205.7	9.6	9.62	100.0
24X	22	0200	205.7-215.4	9.7	9.51	98.0
25X	22	0240	215.4-225.0	9.6	8.02	83.5
26X	22	0330	225.0-234.6	9.6	8.21	85.5
27X	22	0410	234.6-244.2	9.6	9.34	97.3
28X	22	0505	244.2-253.7	9.5	9.10	95.8
29X	22	0620	253.7-263.4	9.7	9.54	98.3
30X	22	0730	263.4-273.1	9.7	10.18	104.9
31X	22	0845	273.1-282.8	9.7	9.70	100.0
32X	22	1000	282.8-292.4	9.6	10.05	104.7
33X	22	1130	292.4-302.0	9.6	9.56	99.6
34X	22	1250	302.0-311.6	9.6	9.99	104.0
35X	22	1410	311.6-321.1	9.5	9.99	105.0
36X	22	1545	321.1-330.7	9.6	10.00	104.1
37X	22	1715	330.7-340.3	9.6	10.07	104.9
38X	22	1830	340.3-349.9	9.6	10.05	104.7
39X	22	1945	349.9-359.5	9.6	8.65	90.1
40X	22	2050	359.5-369.1	9.6	8.79	91.5
41X	22	2200	369.1-378.7	9.6	9.99	104.0
42X	22	2330	378.7-388.4	9.7	9.69	99.9
43X	23	0100	388.4-398.1	9.7	9.92	102.0
44X	23	0245	398.1-407.7	9.6	9.49	98.8
45X	23	0440	407.7-417.3	9.6	9.80	102.0
46X	23	0610	417.3-427.0	9.7	10.17	104.8
47X	23	0810	427.0-436.6	9.6	10.06	104.8
48X	23	0910	436.6-446.2	9.6	7.74	80.6
49X	23	1100	446.2-455.8	9.6	10.11	105.3
50X	23	1220	455.8-465.5	9.7	9.76	100.0
51X	23	1400	465.5-475.1	9.6	9.85	102.0
52X	23	1520	475.1-484.7	9.6	9.83	102.0
53X	23	1725	484.7-494.4	9.7	9.82	101.0
54X	23	1900	494.4-503.9	9.5	10.00	105.2
55X	23	2015	503.9-513.5	9.6	9.80	102.0
56X	23	2130	513.5-523.1	9.6	9.99	104.0
57X	23	2245	523.1-532.7	9.6	9.72	101.0
58X	23	2350	532.7-542.4	9.7	9.95	102.0
59X	24	0130	542.4-552.1	9.7	7.38	76.1
60X	24	0230	552.1-561.6	9.5	9.80	103.0
61X	24	0345	561.6-571.3	9.7	9.75	100.0
62X	24	0530	571.3-580.9	9.6	9.98	104.0
Coring totals:				580.9	583.14	100.4

Note: See also detailed coring summary on the CD-ROM, back pocket, this volume.

tion ranges from a general disrupted sediment appearance, including dispersed darker flecks (pyrite?), silt- or foraminifer-rich blebs and wispy-to-indistinct layering, to well-formed classifiable traces including common *Chondrites* and *Planolites*, less common *Zoophycos*, and many types of rind and halo burrows. Most well-formed cylindrical burrows are horizontal and, in places where burrowing has been intense, the core appears bedded or laminated (Fig. 8). In many places isolated burrows have been infilled by pyrite.

Several minor lithologies are present within Unit I, including hemipelagites that are relatively poor in biogenic components, diatom-bearing sediments, organic-rich layers (ORLs), discrete sand and silt layers, and intraclastic breccia. The minor hemipelagites in-

clude silty clay, clay, and calcareous clayey silt. They have bioturbation, color, and shell fragment and foraminifer contents similar to the major lithologies and occur as gradational alternations, rather than as well-defined beds. A typical composition for silty clay or clay is 71% clay minerals, 10% micrite, 7% calcareous nannofossils, minor proportions of quartz, feldspar, detrital mica, opaque minerals, sedimentary rock fragments, bioclasts, organic debris, volcanic glass shards, and sponge spicules (Sample 979A-26X-1, 115-116 cm).

Diatom-bearing intervals are irregularly present between Section 979A-8H-2, 0 cm (60.0 mbsf) and 41X-5, 70 cm (375.8 mbsf; Fig. 6). They usually occur as discrete green (grayish olive, 10Y 4/2) intervals which have gradational color boundaries with adjacent lithologies. Some calcareous sediments also contain up to 10% diatoms as a minor component. Lithologically, the diatomaceous sediments include mainly nannofossil-diatom ooze and diatom-rich silty clay, but diatom ooze and various combinations of diatoms, nannofossils, sand, silt and clay are also present. The average carbonate content of these intervals is 23%, ranging from 2%-35%. The diatomaceous intervals are characterized by very low magnetic susceptibility (Fig. 9).

At least 29 ORLs of Pleistocene age are present in Hole 979A (Table 2). The lithologies of ORLs include both calcareous and siliceous sediment types. The calcareous lithologies are mainly nannofossil clay to calcareous clay, but include nannofossil-rich clay and silty clay, and nannofossil and calcareous silty clay. The siliceous lithologies range from mixed sediment types such as diatom-rich nannofossil silty clay to diatom ooze. The ORLs range in thickness from <10 cm to >1 m. Total organic carbon concentrations are in excess of 0.8%, and range up to 2.2%, against a background hemipelagic sediment value of 0.5% or less. In addition, fourteen ORLs have been tentatively identified on the basis of lithology and magnetic susceptibility signature within the upper Pliocene in Cores 979A-39X through 61X. The boundaries and TOC values of these ORLs will be determined post-cruise.

Sand- and silt-rich lithologies are present throughout Unit I (Table 3). These lithologies range in texture from silty clay to coarse-grained sand and include a broad spectrum of combinations of clay, silt, and sand. The composition of the silt- and sand-sized fractions of these sediments, as evaluated from smear-slide analysis, typically includes a mixture of biogenic and terrigenous components with variable amounts of glauconite and pyrite (Fig. 10). The biogenic component includes foraminifers, bioclasts, nannofossils, diatoms, and spicules and averages 40% (range of 10%-80%) of the entire sample. The percentage of biogenic components within the silts and sands shows increasing variation with depth, especially below about 150 mbsf. The terrigenous component (quartz + feldspar + mica + rock fragments) averages 18%, with a range of 2%-44% of the entire sample. The proportion of the terrigenous component varies widely with depth over the entire section. The other two important silt- and sand-sized components are glauconite and pyrite. Glauconite averages 5%, ranges from 0% to 50%, and increases slightly, and irregularly, with depth. Pyrite averages 4%, ranges from 0% to 20%, and generally decreases with depth (Fig. 10). Examination of smear slides of these lithologies from Cores 979A-13H through 59X reveals the presence of trace amounts to 1% of volcanic glass shards, particularly in layers rich in the terrigenous component. The shards are colorless to brown and angular to subrounded. Their size is generally in the range from 20-50  $\mu$ m, but shards as large as 200  $\mu$ m are present.

The silt- and sand-rich lithologies are present in beds, laminae, and isolated pockets, and comprise a total thickness of 9.6 m. Average layer thickness is 16 cm, but some beds are as thick as 1.4 m (a sandy silt in Sections 61X-4, 31 cm to 61X-5, 20 cm). Most beds have sharp basal contacts and gradational tops, in places bioturbated. Internally, most are homogeneous and structureless, although some (roughly 20%) are normally graded. Only a few beds are laminated. One bed of calcareous sandy silty clay (Section 19X-1, 22-30 cm; 157.7-158.0 mbsf) is inversely graded.

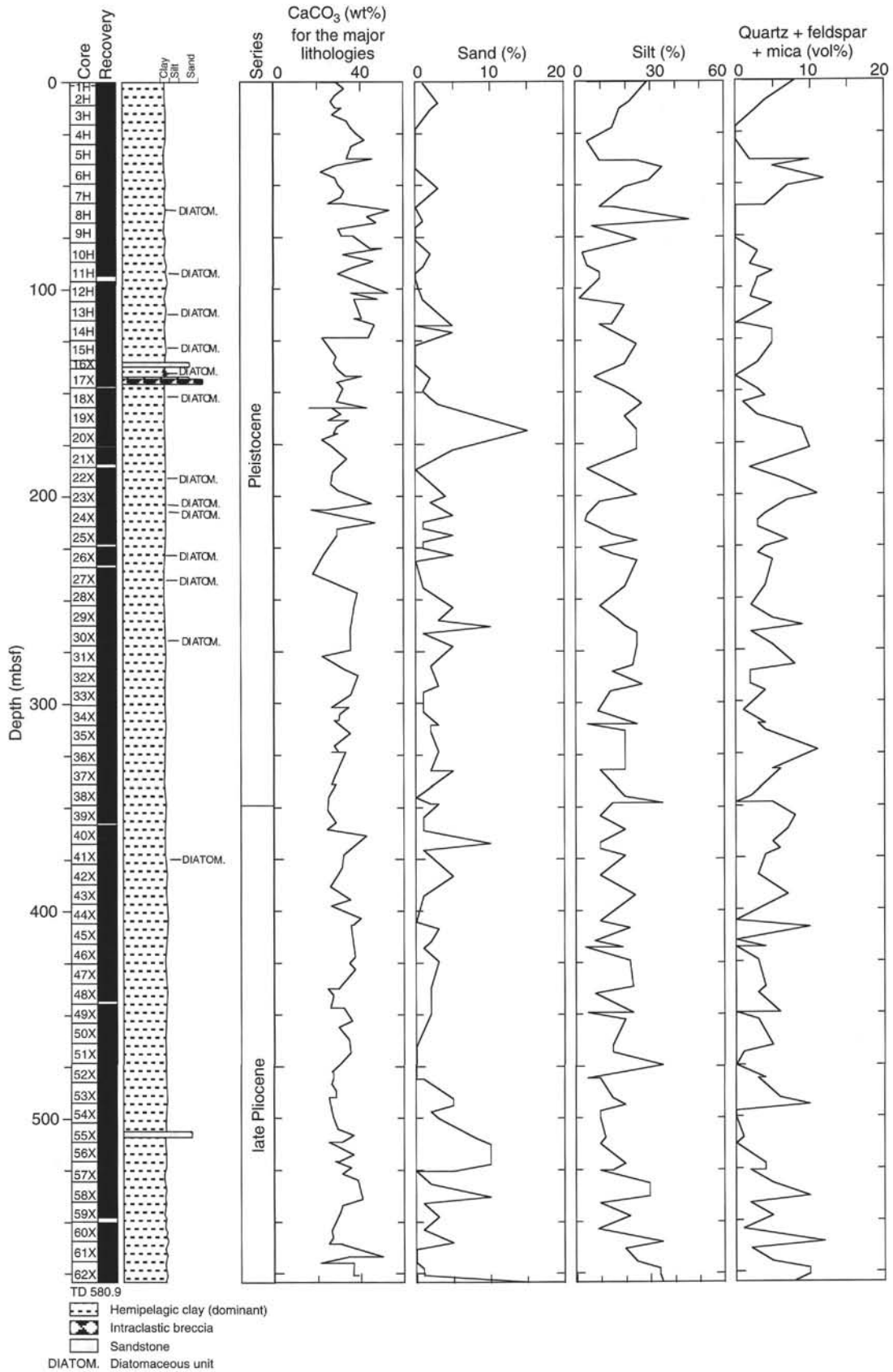


Figure 6. Neogene lithostratigraphy and variation in selected lithologic components for Site 979. Percentages of CaCO<sub>3</sub>, sand, silt, and quartz + feldspar + mica are for the major lithologies only and do not include sand- and silt-rich lithologies.

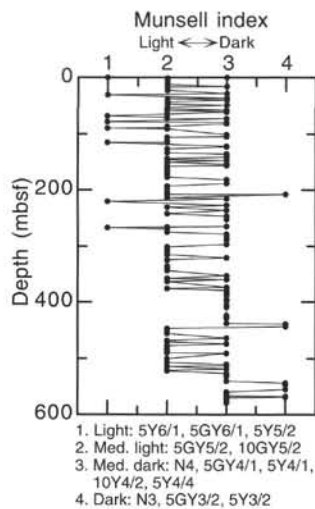


Figure 7. Downhole variation in Munsell color for Site 979.

An interval of intraclastic breccia, probably related to slumping, in Core 979A-17X (Section 17X-3, 87 cm to Section 17X-5, 30 cm; 142.2–144.62 mbsf) contains clasts of grayish olive diatomaceous ooze and light to medium olive gray nannofossil clay in a matrix of nannofossil to nannofossil-rich clay (Fig. 11). The clasts are generally rounded and are commonly deformed and smeared out, and are therefore hard to recognize. The intraclastic breccia is overlain by 41 cm of olive gray to medium dark gray, graded, bioclastic silty sand (Section 17X-3, 46–87 cm; 141.76–142.17 mbsf; Fig. 12).

### Discussion

The sediments of Site 979 are interpreted to have been deposited in an open marine, hemipelagic environment. The dominant nannofossil and nannofossil-rich clays fall between Facies Class E (“silty clays and clays”) and Group G2 (“biogenic muds”) of Pickering et al. (1989, p. 66), which are consistent with continental margin deep marine hemipelagic sedimentation. A deep-water hemipelagic interpretation is further supported by the trace fossil assemblage present in Unit I. The ichnofacies assemblage includes *Chondrites*, *Zoophycos*, and *Planolites*, which together indicate a bathyal (slope) to abyssal (basin plain) environment (Chamberlain, 1978). The nannofossil and pelagic foraminifer components of Unit I were most likely derived by settling from the overlying water column, with minimal lateral transport at the boundary layer. Sedimentation rates at this site are 200 m/m.y. for the Pleistocene and 184–191 m/m.y. for the Pliocene (see “Biostratigraphy” section, this chapter), comparable to, or somewhat higher than, those at the other Alboran Sea sites (see “Biostratigraphy” sections of “Site 976”, “Site 977”, and “Site 978” chapters, this volume).

Silt- and sand-rich layers throughout the sequence display most of the diagnostic characteristics of granular material transported and deposited by turbulent bottom-flowing currents. They have sharp, flat to scoured bases, internal normal grading and gradational tops (e.g., Bouma and Brouwer, 1964), and are interpreted as the deposits of periodic turbidity currents. The presence of both graded and homogeneous layers may indicate variable sorting of sediment in the source area, or winnowing of some of the sand and silt at the site of deposition. The subequal combination of biogenic and terrigenous components in many of the coarse-grained layers, the apparent shallow-water origin of some of the biogenic portion (e.g., shell fragments and echinoid spines), and the recurring presence of glauconite indicate a mixed source area where terrigenous sediment was delivered to a richly biogenic marine platform and then redeposited into slope or

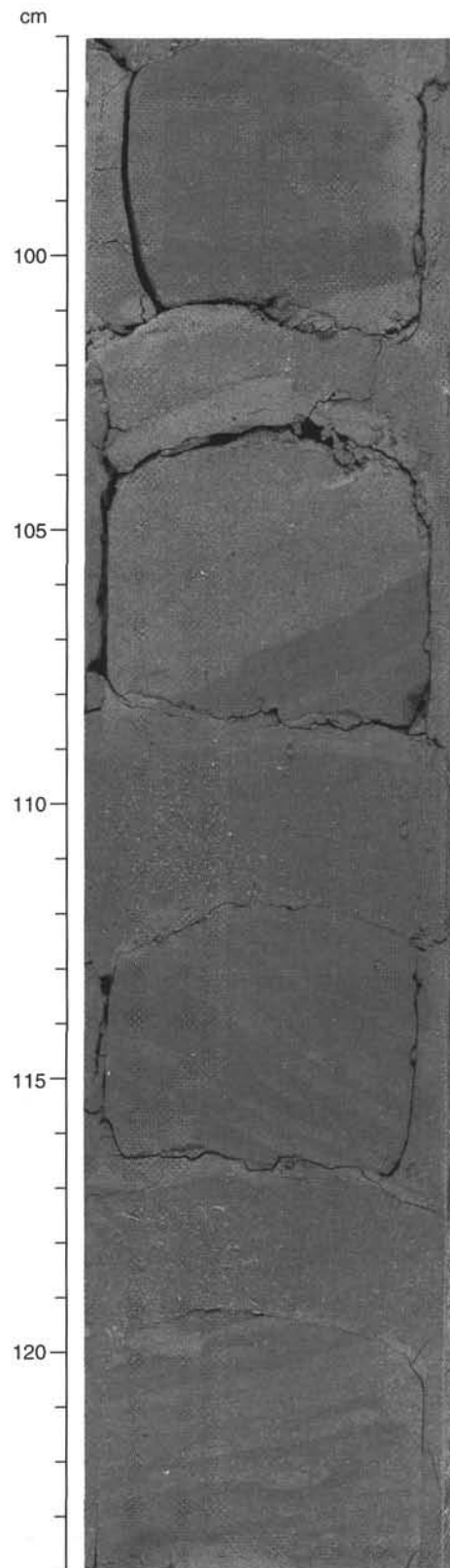


Figure 8. Parallel burrows give the appearance of layering in sediment of Sample 979A-53X-6, 96–124 cm (493.32 mbsf) at 112–125 cm. The inclination of these burrows may be a drilling effect or may reflect actual structural dip. The burrows have similar dip to that of the sand layer from 103–108 cm.

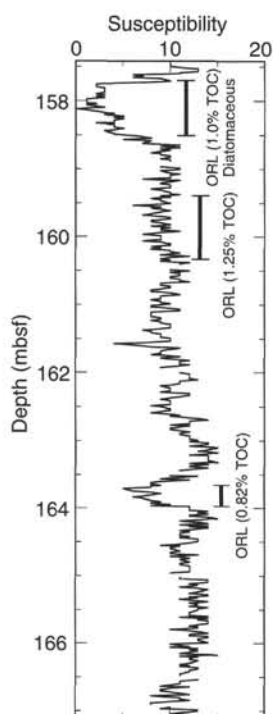


Figure 9. Magnetic susceptibility data for Core 979A-19X. The relative minimum in Section 1 between 157.8 and 158.6 mbsf corresponds to a diatomaceous layer that is also identified as an ORL. Magnetic susceptibility lows downsection between 159.5–160.4 mbsf and 163.7–164.0 mbsf also correspond to ORLs in non-diatomaceous sediment. Susceptibility values must be multiplied by  $0.63 \times 10^{-5}$  to convert to SI units.

basinal environments. No trends are obvious in thickness, composition, or frequency of sand and silt layers.

An unconformity identified on the basis of the micropaleontological faunal assemblage between Sections 979A-51X-CC, 74 cm (475.35 mbsf) and 52X-3, 22 cm (477.46 mbsf) is located in weakly bioturbated to structureless nannofossil-rich clay with no obvious breaks in the record. This suggests that the faunal break may be represented by a period of slow deposition rather than by erosion or non-deposition.

## BIOSTRATIGRAPHY

### Calcareous Nannofossils: Abundance and Preservation

All samples examined from Hole 979A contain abundant calcareous nannofossils. Nannofossil preservation ranges from moderate to good to very good.

### Biostratigraphy

#### Hole 979A (Fig. 13)

The stratigraphic interval recovered in this hole ranges from upper Pliocene (Subzone NN16A) to uppermost Pleistocene–Holocene (NN21B). All zones and subzones from NN16A to NN21B are present. Figure 13 shows the zonal assignments of each core, together with the occurrence in the hole of the species that define the zonal boundaries.

The Pliocene/Pleistocene boundary is approximated by the NN19B/NN19A Subzonal boundary. This boundary occurs between Samples 979A-37X-CC (340.77 mbsf) and 979A-38X-4, 91–93 cm (345.33 mbsf).

Table 2. Location of organic-rich layers in Site 979.

Core, section, interval (cm)	Top (mbsf)	Bottom (mbsf)	TOC (%)	Type
161-979A-				
2H-1, 68, to 2H-2, 121	2.180	4.210	1.37	II
2H-5, 105, to 2H-7, 5	8.550	10.550	1.36	II
2H-7, 28, to 3H-3, 77	10.780	14.770	1.05, 1.65	II
3H-4, 139, to 3H-5, 130	16.890	18.300	0.91	III
3H-6, 119, to 4H-1, 80	19.690	21.300	0.85	III
4H-2, 78, to 4H-4, 72	22.780	25.720	0.90	III
5H-1, 37.5–129	30.375	31.290	0.93	III
7H-3, 19–73	52.190	52.730	1.15	II
7H-4, 109, to 7H-6, 51	54.590	57.010	1.20	II
9H-2, 147, to 9H-3, 65	70.970	71.650	0.94	III
11H-2, 50–62	89.000	89.120	0.82	III
13H-1, 10, to 13H-4, 80	106.100	110.220	1.02	II
13H-6, 8, to 13H-7, 85	112.500	114.770	1.17	II
15H-2, 95, to 15H-3, 50	126.100	127.150	0.91	III
17X-3, 0–40	141.300	141.700	0.82	III
17X-4, 140, to 17X-5, 20	144.200	144.500	1.97	II
18X-2, 124, to 18X-3, 98	150.640	151.880	1.31	II
19X-1, 26–133.5	157.760	158.835	1.00	II
19X-2, 49–139	159.490	160.390	1.25	II
19X-5, 17–49	163.670	163.990	0.82	III
20X-1, 43–139	167.530	168.490	1.13	II
20X-2, 122–140.5	169.820	170.005	2.02	I
20X-3, 62.5–89.5	170.725	170.995	1.27	II
21X-1, 0, to 21X-2, 72	176.800	179.020	0.93	III
22X-3, 10–130	188.490	189.690	2.18	I
27X-7, 0–50	242.490	242.990	0.83	III
30X-3, 91, to 30X-4, 36	266.130	268.030	1.09	II
30X-6, 24–112	269.810	270.690	0.78	III
33X-8, 11, to 33X-CC, 16.5	301.440	301.915	1.66, 1.13	II

Notes: Type designations: I: >2% TOC, II: 2%–1% TOC, III: 1%–0.5% TOC, IV: <0.5% TOC, V: TOC unknown. A single TOC analysis done within each ORL interval and may not be representative of the entire interval. For exact location of TOC analysis, see Table 6, this chapter. This table is also on the CD-ROM, back pocket, this volume.

### Planktonic Foraminifers: Abundance and Preservation

Planktonic foraminifers are abundant and well preserved in most Pleistocene samples in Hole 979A. A few exceptions were observed in Samples 979A-11X-CC (93.6 mbsf), and 28X-CC through 30X-CC (253.25–273.53 mbsf) where preservation of planktonic foraminifers is good, although the sample is richer in neritic benthic foraminifers and associated shelf bioclastic debris, and in Samples 979A-12X-CC (107.03 mbsf) and 23X-CC (243.2 mbsf) where foraminifers are few to absent due to the overwhelming amount of diatomaceous sediment.

Most of the Pliocene samples contain abundant, well-preserved planktonic foraminifers. Exceptions include Samples 979A-39X-CC (358.5 mbsf) and 43X-CC (398.27 mbsf), where fragmentation of the planktonic foraminifers is moderate to severe, Sample 979A-42X-CC (388.86 mbsf) where foraminifers are diluted by the overwhelming amount of diatoms, and Samples 979A-58X-CC (542.6 mbsf) and 59X-CC where preservation is poor and encrustation severe.

### Biostratigraphy

Biozones, the distribution of marker species, and sampling intervals are shown in Figure 14.

#### Hole 979A (Fig. 14)

An upper Pliocene (MPL4b?–MPL5)–Pleistocene sedimentary sequence (698 m thick) was recovered at Site 979.

The Pleistocene is well represented in Samples 979A-1CC (1.41 mbsf) through 979A-33X-CC (301.91 mbsf). The *Globorotalia truncatulinoides excelsa* Zone was recognized from Sample 979A-1H-CC (1.41 mbsf) to 21X-CC (184.72 mbsf), and *Globigerina cariacensis* Zone was recognized between Samples below 979A-22X-CC (195.80 mbsf) and 33X-CC (301.91 mbsf).

**Table 3. List of sand and silt layers within Unit 1 showing depth, thickness, sedimentary characteristics, and the compositions of the silt and sand fractions from smear-slide analyses in Hole 979A.**

Core, section, interval (cm)	Depth (mbsf)	Thickness (m)	Description	Biogenic (%)	Terrigenous (%)	Glauconite (%)	Pyrite (%)
2H-2, 96-98	4.00	0.02	Clayey silty sand; sharp base, gradational top	42	15	10	5
2H-4, 120-130	7.20	0.10	Silty laminated	40	4	0	2
3H-5, 53-60	17.50	0.07	Coarse to fine sand; graded, sharp base, gradational top	50	30	0	0
3H-6, 17-63	18.70	0.46	Glauconite-rich silty sand; medium sand to silt; graded, sharp bases, smeared tops; 4 layers in this interval, total thickness = 16 cm	45	35	5	10
5H-1, 133-134	31.30	0.01	Silty sand sharp base, gradational top	40	35	5	10
5H-6, 19-21	37.70	0.02	Silty sand sharp base, gradational top				
6H-CC, 34-35	49.40	0.01	Silty sand; sharp base, gradational top; composition like Core 5H				
9H-4, 75-77	73.30	0.02	Pyrite-rich sandy clay; sharp base, gradational top	48	12	0	10
10H-4, 78-83	82.80	0.05	Sandy clay; graded, sharp (scoured?) base; gradational, bioturbated top; 2 layers	42	9	0	2
10H-5, 74-77	84.20	0.03	Sandy clay; sharp base, gradational top; discontinuous; composition similar to 10H-4				
10H-7, 9-13	86.60	0.04	Sandy clay; irregular sharp base, gradational top				
11H-1, 102-116	88.00	0.14	Medium to fine sand grades upward to silt; sharp base; coarse bioclastic tail				
11H-5, 73-77	93.50	0.04	Medium to fine sand grades upward to silt; sharp base; coarse bioclastic tail				
12H-5, 130-136	103.00	0.06	Silt-rich nannofossil clay; sharp base, gradational top	37	9	0	5
13H-1, 9-17	106.10	0.08	Silty layer				
13H-CC, 22-25	116.40	0.03	Silty sand	49	32	5	0
14H-6, 14-16	122.30	0.02	Fine sand to sandy silt; irregular sharp base, gradational top				
14H-7, 48-51	124.10	0.03	Sand; graded, sharp base	42	30	5	5
16X-1, 0-73	134.50	0.73	Gravel to silty sand; graded, soupy at top; abundant shell fragments				
17X-3, 46-68	141.80	0.22	Bioclastic silty sand; graded, above intraclastic breccia	60	10	10	1
17X-3, 72-87	142.00	0.15	Bioclastic silty sand; graded, above intraclastic breccia				
19X-1, 22-30	157.70	0.08	Calcareous sandy silty clay; inversely graded	45	17	2	5
23X-2, 112-113	197.50	0.01	Nannofossil- foraminifer-rich clay; sharp base, gradational top	22	8	0	2
24X-2, 69-94	207.90	0.25	Silty clay, structureless to diatom-rich clayey silt	10	27	0	10
24X-4, 118-132	211.40	0.14	Coarse to very coarse sand lag base with sharp base and sharp contact with overlying laminated fine to medium sand	15	31	0	5
26X-2, 14-22	226.60	0.08	Sandy silty clay; parallel to cross laminated	31	35	0.1	1
28X-2, 100-115	246.70	0.15	Calcareous silty clay with shell fragments	25	2	1	20
29X-2, 9-16	254.40	0.07	Glauconite-rich bioclastic sandy silty clay	47	12	10	2
29X-4, 109-116	258.40	0.07	Glauconite-rich bioclastic sandy silty clay				
29X-5, 77-84	259.60	0.07	Glauconite-rich bioclastic sandy silty clay				
29X-5, 137-145	260.20	0.08	Glauconite-rich bioclastic sandy silty clay				
29X-6, 118-120	261.50	0.02	Glauconite-rich bioclastic sandy silty clay				
30X-6, 9-16	269.60	0.07	Glauconite-rich bioclastic sand	55	15	20	5
32X-5, 104-113	288.90	0.09	Calcareous sandy silty clay; graded	55	3	5	2
32X-5, 123-128	289.10	0.05	Calcareous sandy silty clay; graded				
33X-4, 5-25	296.00	0.20	Bioclastic silty sand; medium sand with shell fragments	60	20	5	2
35X-5, 40-53	317.40	0.13	Calcareous silty clay; soupy medium to coarse sand with shell fragments	31	6	1	1
35X-7, 115-121	321.10	0.06	Calcareous silty clay; soupy medium to coarse sand with shell fragments				
36X-5, 118-125	328.00	0.07	Blackish disrupted sand with shell fragments				
37X-CC, 19-22	340.60	0.03	Calcareous silty sandy clay; medium to coarse sand, disrupted	50	10	2	3
40X-3, 22-31	362.70	0.09	Sand- and silt-rich layers; no cohesion				
40X-3, 95-144	363.50	0.49	Sand- and silt-rich layers; no cohesion				
40X-5, 110-116	366.50		Sand- and silt-rich layers; no cohesion				
41X-2, 0-40	370.60	0.06	Foraminifer-rich bioclastic sand; fine-medium sand, no cohesion	70	12	50	0
43X-4, 54-55	392.80	0.40	Calcareous sand; medium-fine sand; graded, sharp base, bioturbated top	37	43	5	5
43X-6, 64-75	395.90	0.01	Calcareous sand; medium-fine sand; graded, sharp base, bioturbated top				
46X-3, 90	420.70	0.11	Foraminifer-rich interval				
46X-3, 94-96	420.70	0.01	Foraminifer-rich interval				
47X-6, 129-131	435.00	0.02	Glauconitic fine sandstone	27	30	20	3
53X-6, 100-110	493.20	0.10	Very fine sand, inclined bed; sharp top and base				
53X-6, 110-150	493.30	1.20	Nannofossil sandy silty clay	24	5	0	0.1
53X-7 and CC			Nannofossil sandy silty clay				
54X-3, 122-132	498.60	0.10	Calcareous sand; laminated	80	12	3	0.1
54X-4, 0-9	498.70	0.09	Fine sand, structureless				
54X-4, 36-44	499.10	0.08	Silt, soupy				
55X-4, 120-150	509.60	0.30	Very fine to fine homogeneous sand; graded at top				
55X-5, 51-54	510.40	0.03	Foraminifer sand				
60X-4, 112, to 60X-5, 53	557.70	0.91	Glauconite-rich sandy siltstone; graded from medium sand at base to sandy silt at top				
61X-4, 31, to 61X-5, 20	566.40	1.39	Sandy siltstone graded from fine to medium sand up to silt	25	8	0	0
62X-1, 17-19	571.50	0.02	No description				
62X-5, 34-49	577.40	0.15	Calcareous clayey silt	10	15	0.1	0.1

Note: Percentages of components refer to the entire sample, not just to the silt and sand fraction.

The Pliocene is represented by biozones MPL6-MPL5a in Samples 979A-34X-CC (311.94 mbsf) through 62X-CC (581.28 mbsf). *Globorotalia bononiensis* is consistently present down to Sample 979A-61X-6, 68-70 cm (569.78 mbsf). Zone MPL4b, defined by the last occurrence of *Sphaeroidinellopsis seminulina*, was not reached.

### Benthic Foraminifers

Benthic foraminifers at Site 979 (present-day water depth 1062.1 m) are larger in size and more abundant than at any other Leg 161 site. The *Cassidulina/Islandiella/Globocassidulina* group are particularly well represented. The benthic foraminifers are diagnostic of

lower epibathyal (500-1300 m) to upper mesobathyal (1000-1800 m) depths as defined by Wright (1978). They generally comprise <1%-2% of the total foraminiferal assemblage, except where there is evidence for downslope contamination by shelf taxa that are often abraded and mixed with deeper water assemblages. A significant degree of downslope contamination was observed throughout the hole.

### Biozonal Correlation

Correlation of the calcareous nannofossil and planktonic foraminiferal zonations for Hole 979A is shown in Figure 15.

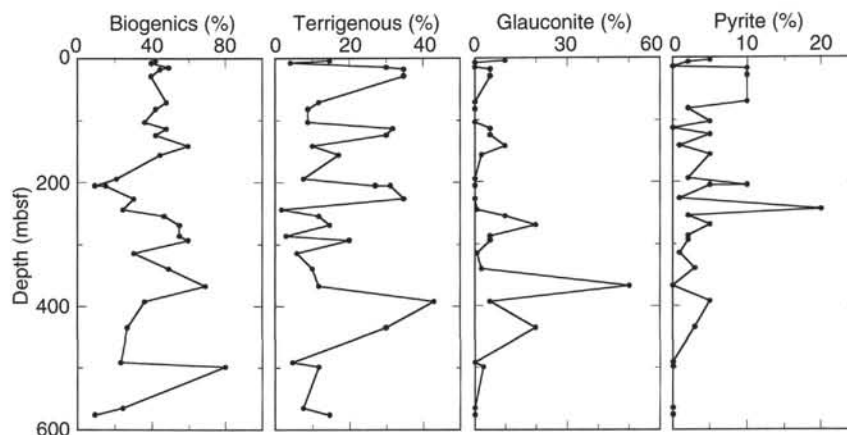


Figure 10. Downhole variation in selected components for sand- and silt-rich lithologies. Percentages determined by visual estimation from smear slides. Biogenics = (nanofossils + foraminifers + bioclasts + diatoms + spicules); Terrigenous = (quartz + feldspar + mica + rock fragments).

### Paleoenvironment

Planktonic and benthic foraminifers and calcareous nanofossils are indicative of an open-marine environment with calcareous plankton dominating over benthic microfossils. However, the regular presence of echinoid spines and neritic benthic foraminifers suggests various episodes of input from shallower waters.

### Sedimentation Rates

Figure 16 shows the sedimentation rate for Hole 979A. Age data used for calculations (Table 4) are based on first and last appearance events of selected nanofossils and planktonic foraminifers. Average sedimentation rate in Hole 979A was 200 m/m.y. for the Pleistocene, and 184–191 m/m.y. for the upper Pliocene. The disappearance at the same level of *G. bononiensis* (14) and *Discoaster pentaradiatus* (15) might indicate a short hiatus within the upper Pliocene. Below this level, there is an increase in sedimentation rates to 696 m/m.y.

### PALEOMAGNETISM

Fifty-six APC and XCB cores were measured with the cryogenic magnetometer. Blanket AF demagnetization was routinely applied at 15 mT. Some archive sections were progressively demagnetized up to 30 mT. APC cores were oriented with the Tensor tool (Table 5).

### Remanent Magnetization

Intensities of remanent magnetization are about  $10^{-3}$  A/m before demagnetization and  $10^{-4}$  A/m after AF demagnetization (15 mT). Remanent directions seem to be extensively overprinted. Declinations show an unusual distribution, that is, before the demagnetization they are scattered and only weakly clustered around  $45^\circ$  from  $100$  to  $350$  mbsf; after demagnetization they cluster tightly around  $200^\circ$  throughout the hole (Fig. 17). As the clustered declinations are observed only after AF demagnetization, two different explanations might be possible. Removing a less coercive overprint, such as viscous remanent magnetization at 15 mT, may allow a more coercive overprint to dominate magnetization and align to  $200^\circ$ . This means that the overprint is almost antiparallel to the radial remagnetization (PRR) observed at the other sites (Sites 974, 975, 976, and 978) and may be another type of remagnetization. Another more likely explanation may be the acquisition of anhysteretic remanent magnetization (ARM) from the AF demagnetization. Spurious magnetizations parallel to the X-axis were frequently observed at this site when the progressive AF demagnetization was performed on archive halves (Fig. 18). The same type of demagnetization behavior has been observed

occasionally during this cruise (see Fig. 39 in the “Site 976” chapter). Core samples were demagnetized by being passed through three demagnetizing coils (X, Y, and Z) sequentially. A very small imbalance between those coils could impart spurious ARM on samples.

Re-oriented declinations of APC cores using the Tensor tool data are not very helpful in determining declinations (Fig. 19). Before AF demagnetization, inclinations are mostly steep and have positive values (about  $80^\circ$ ), indicating a steep positive overprint throughout the core. After the demagnetization at 15 mT, mean inclination decreases to about  $60^\circ$  with sporadic negative values (Fig. 17). However, it is impossible to identify any polarity zones at this site.

### Periodicity of Magnetic Susceptibility

In Figure 20, an apparent periodicity of low-field susceptibility is shown for the interval between 0 to 55 mbsf, which is not related to any significant change in lithology or any kind of contamination. Based on the preliminary biostratigraphic data, one of these periodicities could correspond to one of the climatic periodicities at 21 ky. See “Physical Properties” section (this chapter) for general trend of the magnetic susceptibility.

### STRUCTURAL GEOLOGY

Site 979 is located south of the Alboran Ridge in the Southern Alboran basin. The Alboran Ridge has a strongly faulted northern margin, and it has been tilted significantly to the south during the Pliocene to Pleistocene. The Pliocene to Pleistocene sediments on the southern flank of the ridge have been progressively tilted and folded, and there are at least two unconformities within the sequence, which become more profound northward toward the crest of the ridge. Deformation in this area has probably continued to the present day. Site 979, however, was located in a flat-lying Pliocene to Pleistocene sequence south of this zone of active deformation.

The Pliocene to Pleistocene sediment recovered from Site 979 is for the most part horizontal, but there are local variations in dip that probably result from slump folding. These zones of dipping beds occur in Core 979-19X (maximum apparent dip  $50^\circ$ ), 45X (maximum apparent dip  $68^\circ$ ), and 53X (maximum apparent dip  $25^\circ$ ). Because of the sediment softness and the intense drilling-induced disturbance, it was not possible to determine dips in three dimensions or to reconstruct the structures responsible for these dip variations.

Cores 979-42X through 53X show a variably developed and variably oriented fissility oblique to the bedding, and, in addition, they show fractures parallel to the core. Neither feature was easy to study because of the rotation of the “biscuits” produced by drilling, the softness of the sediment, and its tendency to smear along the cut surface,

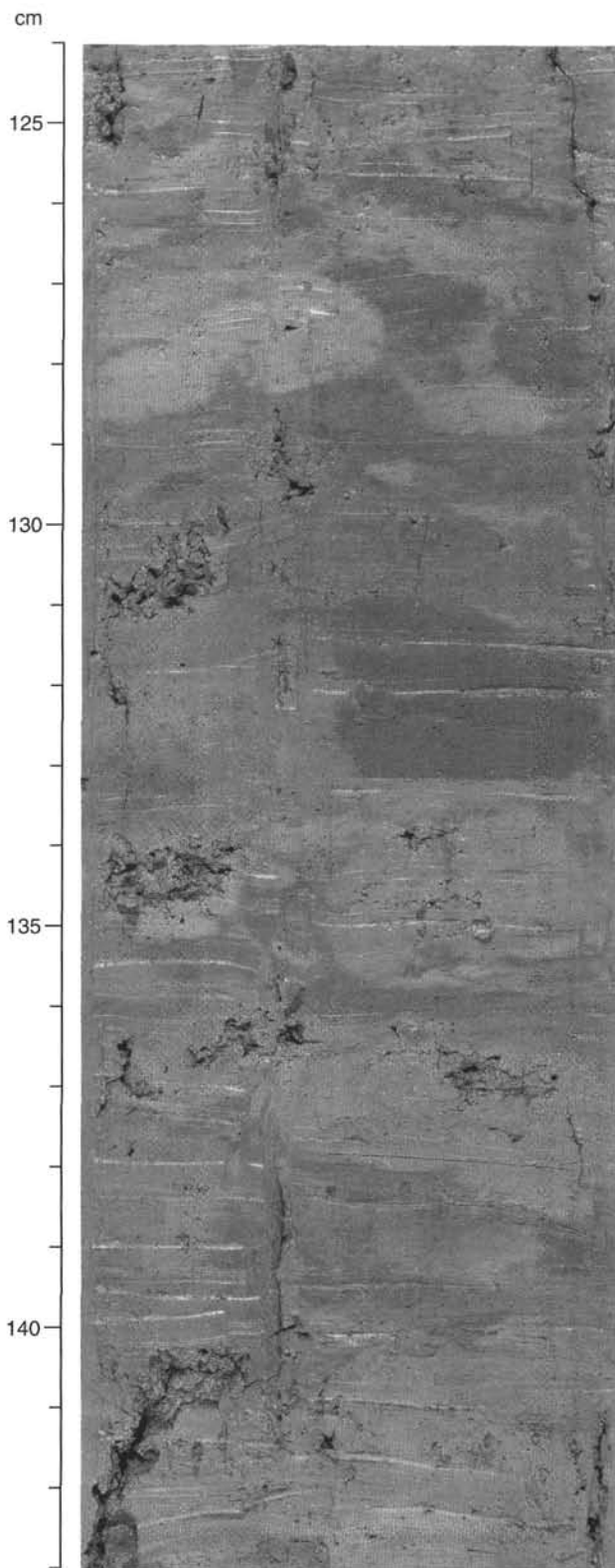


Figure 11. Intraclastic breccia (Sample 979A-17X-3, 124–143 cm; 142.54 mbsf) showing poorly defined, rounded clay intraclasts supported in a clay matrix. The darker clast on the right side of the core from 131 to 133 cm is diatomaceous, whereas the surrounding clay is not.

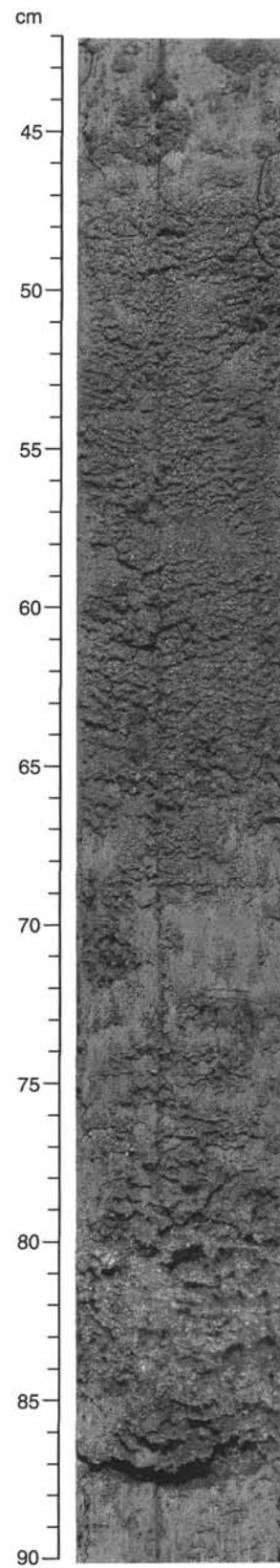


Figure 12. Graded bioclastic silty sand overlying the breccia in Sample 979A-17X-3 shown in Figure 11. Base located at 87 cm, top at 46 cm.

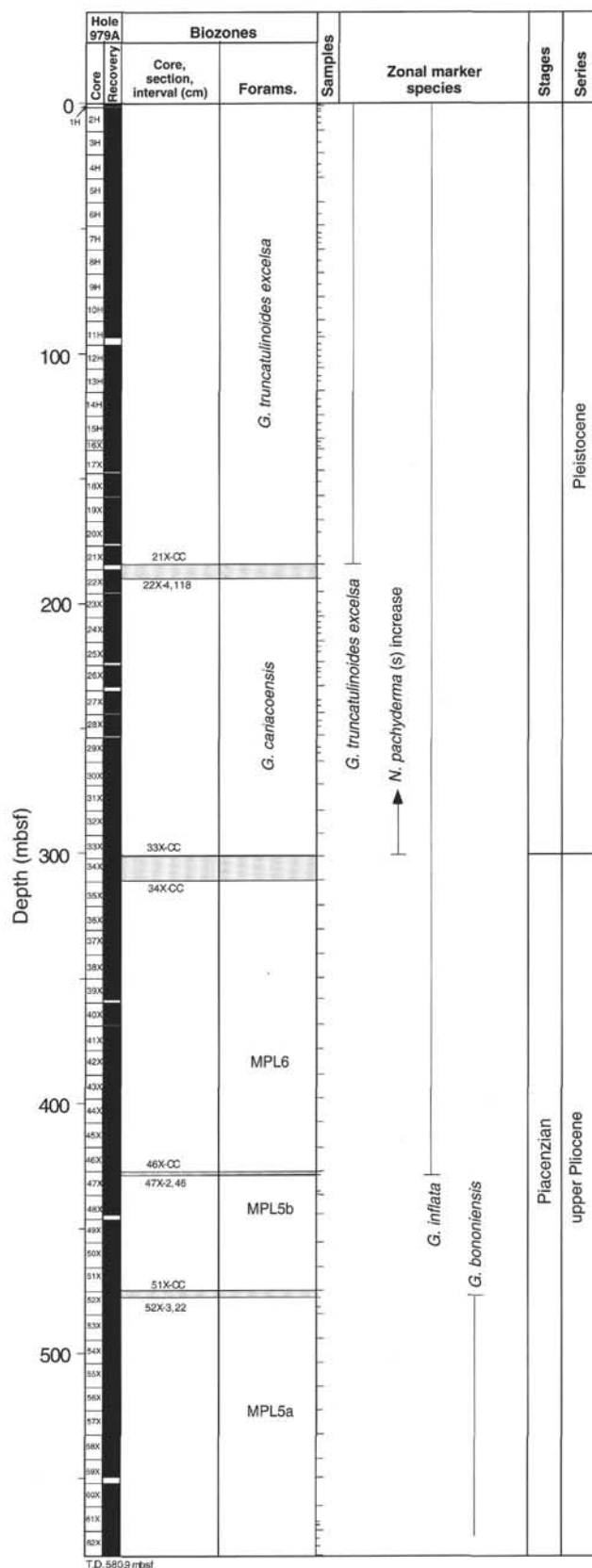
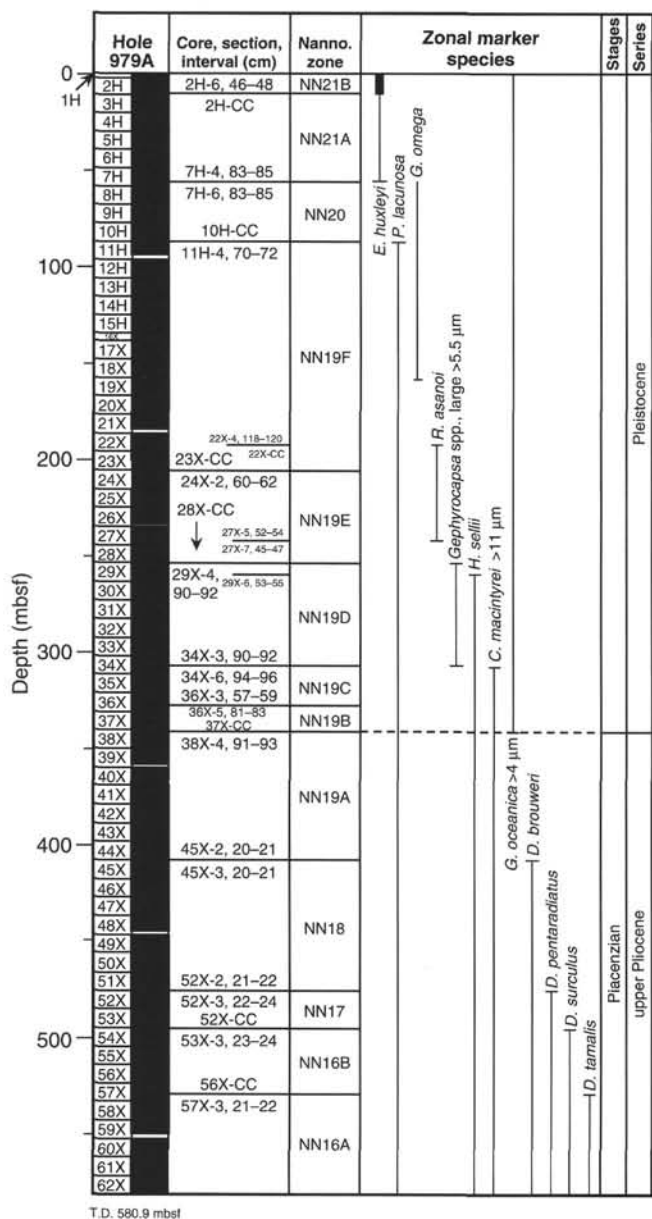


Figure 13. Calcareous nannofossil zonation of Hole 979A. Bold lines represent acme intervals.

which effectively obscures the fissility. Some or all of the vertical fracturing is likely to have been induced at some time during the drilling and coring. The fissility appears to be an incipient disjunctive cleavage, and may be a response to deformation associated with the nearby Alboran Ridge. Post-cruise studies of the magnetic anisotropy may provide more information about the strain associated with this fabric.

### ORGANIC GEOCHEMISTRY

Calcium carbonate and organic carbon concentrations were measured on samples obtained regularly from Hole 979A. Organic matter atomic C/N ratios and Rock-Eval analyses were employed to determine the type of organic matter contained within the sediments. Ele-

Figure 14. Planktonic foraminiferal zonation of Hole 979A. Shaded areas represent intervals not sampled.

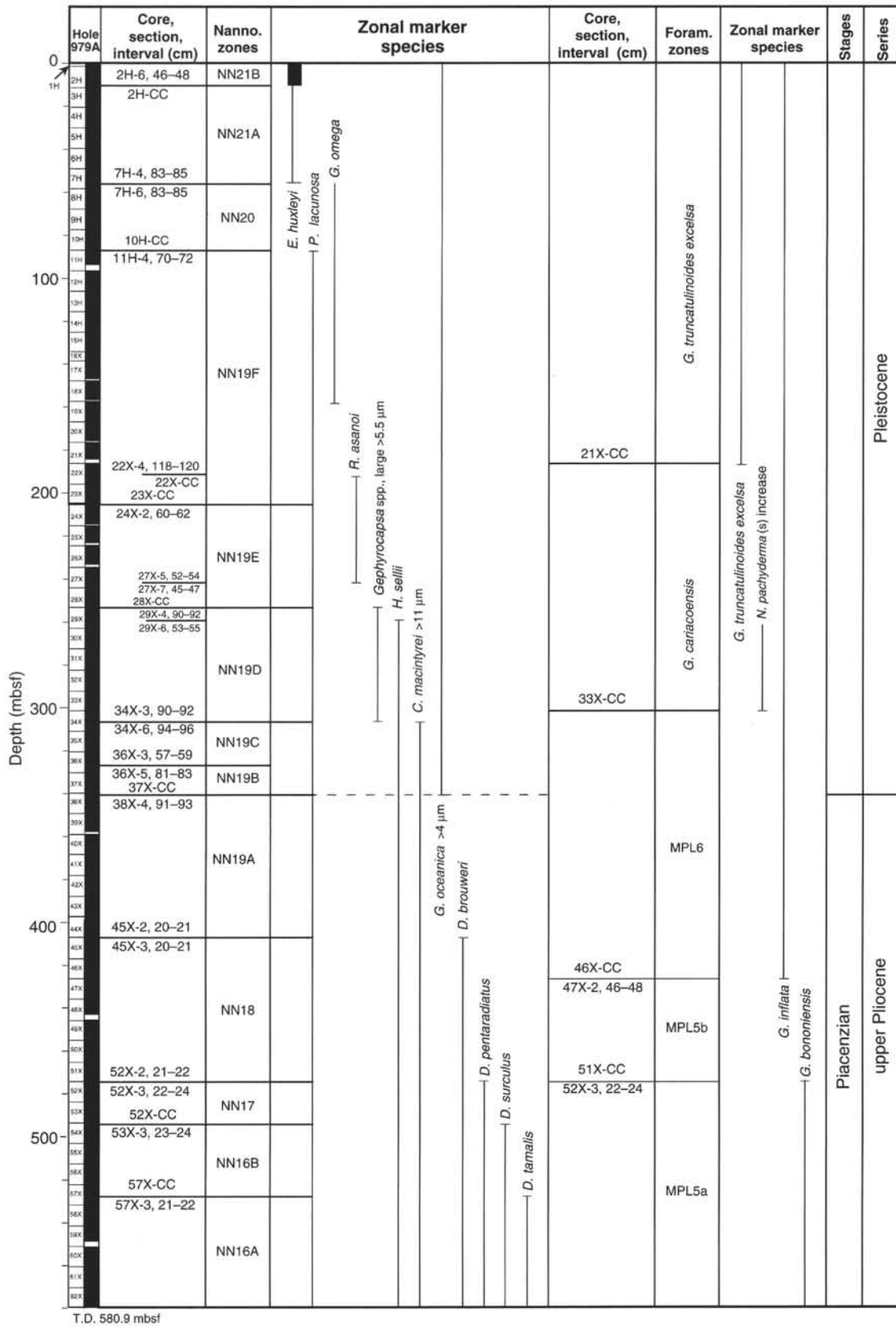


Figure 15. Summary of nannofossil and foraminiferal zonation of Hole 979A.

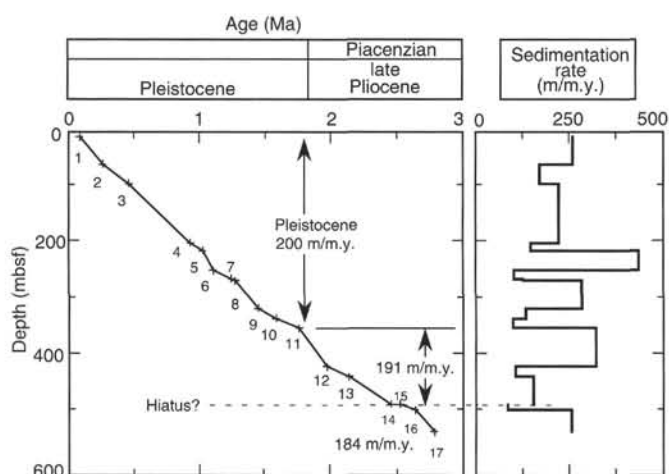


Figure 16. Sedimentation rates at Hole 979A.

vated amounts of headspace gases were encountered, and routine monitoring of these gases was done for drilling safety.

### Inorganic and Organic Carbon Concentrations

Concentrations of carbonate carbon vary from 0% to 8.3% in Site 979 sediments (Table 6; Fig. 21). These carbonate carbon concentrations are equivalent to 2% to 69% sedimentary  $\text{CaCO}_3$ , assuming that all of the carbonate is present as pure calcite. The range in carbonate content reflects varying combinations of fluctuating biological productivity, dilution by non-carbonate sedimentary components, and post-depositional carbonate dissolution driven by oxidation of organic carbon during Pliocene–Pleistocene times.

Sediments at Site 979 average 0.7% TOC, which is more than twice the deep-sea average of 0.3% compiled by McIver (1975) from DSDP Legs 1 through 33. TOC concentrations fluctuate between 0% and 2.0% (Table 6; Fig. 21). The elevated TOC concentrations of the sediments at Site 979 probably are a consequence of high sedimentation rates (see “Lithostratigraphy” section, this chapter), which improve organic matter preservation (e.g., Emerson and Hedges, 1988).

### Organic Matter Source Characterization

Organic C/N ratios were calculated for Site 979 samples using TOC and total nitrogen concentrations to help identify the origin of their organic matter. Site 979 C/N ratios reach as high as 20, but most are between 4 and 8 (Table 6), which is representative of algal organic matter (e.g., Emerson and Hedges, 1988; Meyers, 1994).

The C/N ratios of 22 samples containing a minimum of 1% TOC average 11.0, which is a value that is intermediate between unaltered algal organic matter and fresh land-plant material. It is likely that these organic-carbon-rich sediments contain partially degraded algal material with some admixed continental organic matter. Preferential loss of nitrogen-rich, proteinaceous matter can elevate the C/N ratios of algal organic matter during settling to the seafloor.

Sediment samples having relatively elevated TOC concentrations (>0.5%) were selected for Rock-Eval characterization of the type and thermal maturity of their organic matter contents (Table 7). A van Krevelen-type plot of the hydrogen index and oxygen index values suggests that the sediments contain a mixture of some Type II (algal) and mostly Type III (land-derived) organic matter (Fig. 22). This source assignment for the organic matter conflicts, however, with the relatively low C/N ratios for these samples, which indicate that the organic matter is predominantly marine material. The contradiction between the Rock-Eval source characterization and the elemental

source characterization is evidence that the marine organic matter has been oxidized, probably by microbial reworking (Espitalié et al., 1977).

### Headspace Gases

Concentrations of headspace methane are elevated in sediments from Hole 979A (Fig. 23). Two sources of the gas are possible. First, gas from some deeper origin may have migrated into the sediments. Evidence for migration of methane into porous sediments from deeper sources has been found at Sites 762 and 763 on the Exmouth Plateau (off northwest Australia), where a known thermogenic source exists in underlying Jurassic rocks (Meyers and Snowdon, 1993). No comparable source of gas is known on the southern margin of Iberia. A second possibility is in situ formation by methanogenic bacteria. High  $\text{C}_1/\text{C}_2$  ratios (Table 8) indicate that the methane is biogenic, as opposed to thermogenic, in origin. The source of the methane is probably from in situ microbial fermentation of the marine organic matter present in the sediments at Site 979. Similar microbial production of methane from marine organic matter has been inferred from high biogenic gas concentrations in Pliocene–Pleistocene sediments from Site 532 on the Walvis Ridge (Meyers and Brassell, 1985), Sites 897 and 898 on the Iberian Abyssal Plain (Meyers and Shaw, in press), Sites 976, 977, and 978 nearby in the Alboran Sea (this volume), and also in middle Miocene sediments from Site 767 in the Celebes Sea (Shipboard Scientific Party, 1990). A biogenic origin of the methane is supported by the disappearance of interstitial sulfate at approximately the same sub-bottom depth where methane concentrations begin to rise (see “Inorganic Geochemistry” section, this chapter). As noted by Claypool and Kvenvolden (1983), the presence of interstitial sulfate inhibits methanogenesis in marine sediments.

Higher molecular weight thermogenic headspace gases are also present at Site 979. Concentrations of propane, the only heavier gas quantitatively measured, exceed those of ethane in sediments below about 300 mbsf and exceeds 100 ppm at the bottom of Hole 979A (Table 8). Ethane is typically the second most abundant component of biogenic gases (Claypool and Kvenvolden, 1983). The gas compositions are therefore unusual and suggest that the propane was produced by thermal degradation of sedimentary organic matter during some former period of elevated heat flow in this sub-basin of the Alboran Sea.

## INORGANIC GEOCHEMISTRY

Twenty-three interstitial water samples were obtained from Site 979 between 5.95 and 554.95 mbsf (Table 9). One sample was taken every core from the second to the sixth core, and one sample every third subsequent core. The interstitial profiles (Fig. 24–27) are influenced by two main processes: early diagenesis of organic matter and the presence of a saline brine at depth. A third minor process is carbonate diagenesis.

### Carbonate Diagenesis

The alkalinity concentration peaks at 16 mM 24.96 mbsf, decreasing below this depth to less-than-seawater values from 412.10 mbsf to the base of the cored interval (Fig. 24B). The alkalinity peak probably reflects the early breakdown of organic matter. The low alkalinity at the base of the cored interval suggests limited precipitation of carbonate and/or formation of zeolite. The calcium profile is dominated by a flux of calcium from depth (Fig. 24C). In contrast, magnesium decreases from near-seawater concentrations at the top of the hole to a minimum of 45 mM at 43.95 mbsf (Fig. 24D). Magnesium concentrations then increase to a maximum at 295.78 mbsf and then decrease slightly toward the base of the hole. The combination of the

**Table 4. Age of calcareous nannofossil and planktonic foraminiferal biostratigraphic events and depth of their occurrence in Hole 979A.**

Biostratigraphic event			Age (Ma)	Depth (mbsf)		
				Top	Bottom	Mean
1	Base	<i>E. huxleyi</i> acme	0.085	9.46	11.51	10.485
2	FO	<i>E. huxleyi</i>	0.26	54.33	57.83	56.08
3	LO	<i>P. lacunosa</i>	0.46	87.63	92.2	89.915
4	LO	<i>R. asanoi</i>	0.93	191.07	195.8	193.435
5	FO	<i>G. omega</i> >4.0 $\mu$ m	1.02	205.72	207.8	206.76
6	FO	<i>R. asanoi</i>	1.1	240.01	242.94	241.47
7	LO	<i>Gephyrocapsa</i> spp. >5.5 $\mu$ m	1.24	253.3	258.26	255.78
8	LO	<i>H. sellii</i>	1.27	258.26	260.89	259.575
9	FO	<i>Gephyrocapsa</i> spp. >5.5 $\mu$ m	1.44	305.26	309.75	307.505
10	LO	<i>C. macintyrei</i> >11 $\mu$ m	1.58	324.55	327.59	326.07
11	FO	<i>G. oceanica</i> >4.0 $\mu$ m	1.75	340.77	345.33	343.05
Pliocene/Pleistocene boundary			1.83	(calculated)		355.83
12	LO	<i>D. brouweri</i>	1.96	409.40	410.91	410.16
13	FO	<i>G. inflata</i>	2.13	427.47	428.19	427.83
14	LO	<i>G. bononiensis</i>	2.45	475.35	477.46	476.405
15	LO	<i>D. pentaradiatus</i>	2.52	475.94	477.46	476.71
16	LO	<i>D. surculus</i>	2.63	484.93	487.94	486.43
17	LO	<i>D. tamalis</i>	2.78	523.49	526.32	524.19

Notes: FO = first occurrence, LO = last occurrence; also indicated are the main chronostratigraphic boundaries. The depth of the Pliocene/Pleistocene boundary is calculated based on dated bioevents and differs from the biostratigraphic approximation of the boundary based on nannofossils. This table is also on the CD-ROM, back pocket, this volume.

**Table 5. Azimuthal orientation of APC cores from Hole 979A using the Tensor tool data.**

Core	Magnetic toolface (MTF) ( $^{\circ}$ )
3	352
4	322
5	306
6	6
7	358
8	189
9	124
10	213
11	177
12	295
13	223
14	272
15	255

Note: The orientation parameter (MTF) is an angle between true north and x-axis of the core-coordinate.

low magnesium concentrations in the upper part of the cored interval and the increased alkalinity suggests that precipitation of high magnesium calcite or dolomite occurs. Strontium concentrations increase in a linear manner from seawater concentrations at the top of the cored interval to 3 mM at the base of the cored interval (Fig. 25C). Such concentrations are about thirty-four times higher than seawater concentrations. The linear nature of the strontium profile indicates a flux of strontium from depth. This is likely to be caused by calcium carbonate recrystallization, which releases strontium to the interstitial phase (Manheim and Sayles, 1974).

### Organic Matter Degradation

The high sediment accumulation rates at this site (200 m/m.y. for the Pleistocene; see "Biostratigraphy" section, this chapter) bury organic matter more rapidly than dissolved oxygen can diffuse from the overlying seawater. Below the depth of oxygen penetration, bacterial degradation of organic matter proceeds sequentially through utilization of nitrate, manganese and iron oxyhydroxides, sulfate, and finally carbon dioxide.

This process is reflected in the sulfate profile, which decreases from seawater concentrations to zero at 24.95 mbsf (Fig. 26A). Below this depth, organic matter degradation occurs by fermentation, as evidenced by the rapid increase in CH<sub>4</sub> concentrations below the zone

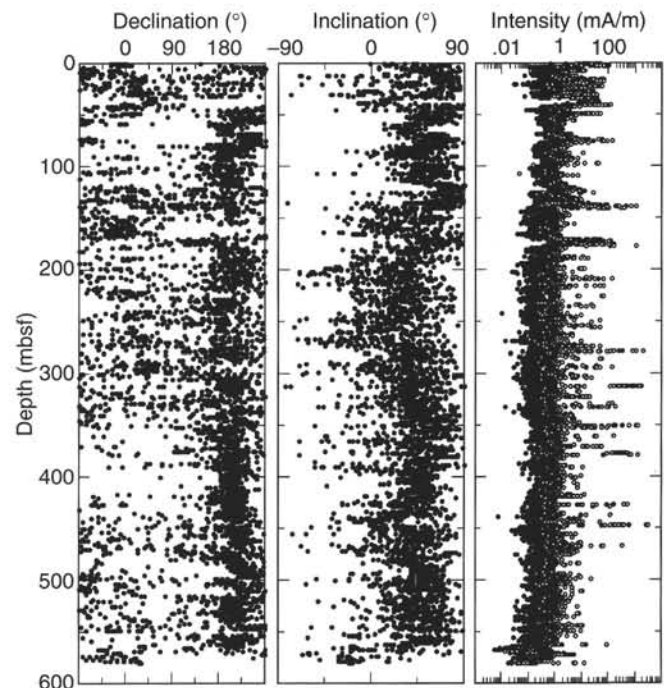


Figure 17. Declination (core-coordinate), inclination, and intensity after 15 mT AF demagnetization for Hole 979A. Open circles on the intensity diagram indicate intensity before demagnetization.

of sulfate reduction (see "Organic Geochemistry" section, this chapter). The higher free energy yield from sulfate reduction ensures that methanogenesis only occurs when sulfate is depleted (Claypool and Kvenvolden, 1983). The manganese profile, however, does not complement the sulfate profile; manganese should peak and then drop to zero before sulfate reduction occurs. The manganese profile, which alternates between 5 and 15  $\mu$ M (Fig. 26B), may reflect relict peaks or the presence of manganese carbonates.

The early degradation of organic matter is evidenced by the phosphate profile (Fig. 27B) as well as the alkalinity profile. Phosphate concentrations reach a peak of 77  $\mu$ M at 24.95 mbsf and then de-

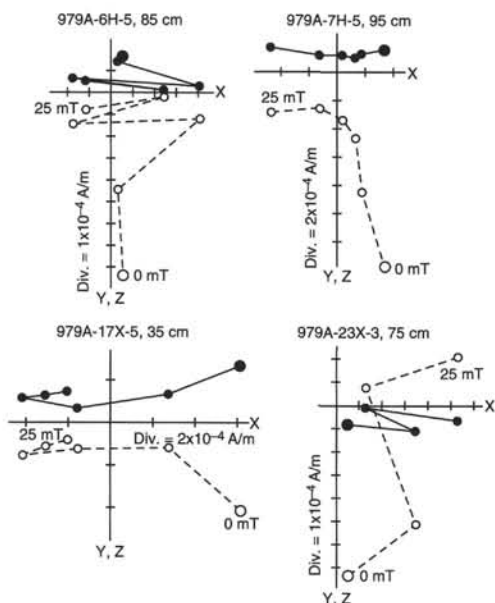


Figure 18. Typical examples of progressive AF demagnetization suggesting spurious ARM acquisition along X and  $-X$  directions by using the degauser equipped with cryogenic magnetometer. Open (solid) symbol indicates projection of vector end-point on vertical (horizontal) plane.

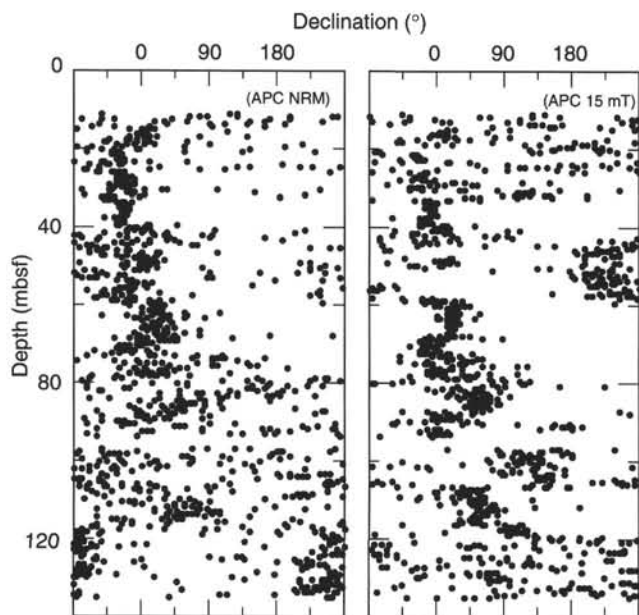


Figure 19. Reoriented declination by using Tensor tool data (Table 5) for APC cores before and after AF demagnetization.

crease rapidly below that depth. Concentrations, however, remain above  $5 \mu\text{M}$  down to 500 mbsf. The phosphate concentrations are unusually high for these sub-bottom depths. Both the alkalinity and phosphate peaks identify the zone of maximum organic matter degradation. Ammonium concentrations increase from 0.69 mM at 5.95 mbsf to 13 mM at the base of the cored interval (Fig. 27A). The ammonium concentrations are also unusually high. The decrease in the ammonium gradient toward the base of the cored interval reflects ion-exchange reactions with clay minerals. These reactions release lithi-

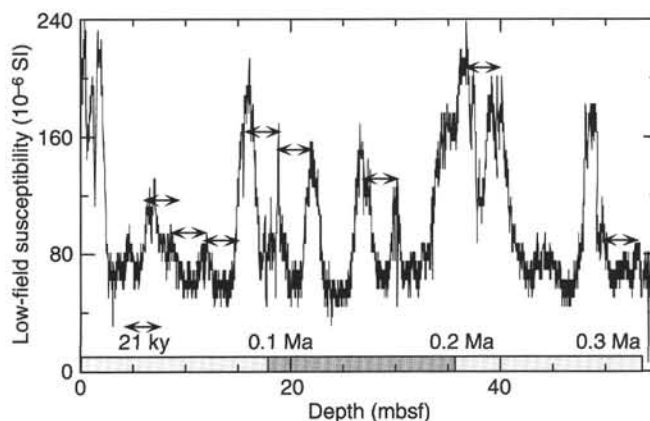


Figure 20. Magnetic susceptibility vs. depth (mbsf) in the upper part of the Hole 977A. Time scale is for reference only and does not correspond to well-dated events. Note apparent periodicity (21 k.y.) in low-field susceptibility between 0 to 55 mbsf.

um; however, an additional source of lithium is required to explain the high lithium concentrations.

### Evaporite-Related Fluxes

The linear increase in calcium, salinity, chlorine, sodium, and, to a degree, lithium (Figs. 24C, 25A–D, and 26D) indicate a deep source for these elements. The constant salinity in the upper section of the cored interval can be accounted for by salinity consumption during sulfate reduction. The conservative nature of chlorine should ensure that interstitial chlorine profiles are only affected by fluid diffusion and advection processes; such behavior can be used to constrain the end-member composition of any brine present. If the brine originated from halite dissolution it would have a sodium/chlorine molar ratio (Na:Cl) of nearly one. The Na:Cl of the interstitial waters decreases from near-seawater ratios at the top of the cored interval to 0.77 to 0.8 below 100 mbsf. These ratios indicate the brine is not from halite dissolution. The calcium profile suggests instead that the brine may originate from gypsum dissolution; similarly, the lithium profile suggests the brine may originate from dissolution of late-stage evaporites. Potassium concentrations decrease from slightly higher than seawater concentrations in the upper section of the cored interval to approximately half seawater concentrations at the base of the cored interval. This pattern is typical for potassium in marine sediments and reflects potassium uptake into clay minerals. Such a profile also indicates that the brine does not originate from dissolution of potassium-bearing salts.

Messinian evaporites are not thought to be present in this region; however, large salt domes are developed on the Habibas Escarpment along the Algerian Margin to the west of Site 979 (Mauffret et al., 1987). Furthermore, the Algerian Basin is thought to be surrounded by a thin salt layer (Mauffret et al., 1992). The dissolution of these salt deposits would provide a possible source for the evaporite-related fluxes present at Site 979. Brines would be able to migrate along basement contacts and fault zones as well as by lateral diffusion through the sediments.

### Silica

Interstitial silica concentrations are variable but exhibit an overall decreasing trend toward the base of the cored interval. Two peaks in the trend exist at 152.35 and 266.57 mbsf. The peaks reflect increases in siliceous sedimentary components at these intervals (see "Litho-

Table 6. Results of inorganic and total carbon (TC) analyses of Pliocene–Pleistocene sediment samples from Site 979.

Core, section, interval (cm)	Depth (mbsf)	Inorg. C (wt%)	CaCO <sub>3</sub> (wt%)	TC (wt%)	TOC (wt%)	TN (wt%)	TS (wt%)	C/N
161-979A-								
1H-1, 9–10	0.09	2.57	21.4	3.43	0.86	0.14	0.00	7.17
1H-1, 60–61	0.60	3.62	30.2	4.55	0.93	0.13	0.05	8.35
1H-CC, 10–11	1.38	3.50	29.2	4.45	0.95	0.12	0.07	9.24
2H-2, 10–11	3.10	3.93	32.7	5.30	1.37	0.15	0.05	10.66
2H-3, 25–26	4.75	3.46	28.8	4.04	0.58	0.09	1.51	7.52
2H-6, 75–76	9.75	3.15	26.2	4.51	1.36	0.18	2.37	8.81
2H-CC, 14–15	11.34	3.45	28.7	4.50	1.05	0.15	1.42	8.17
3H-2, 50–51	13.00	3.80	31.7	5.45	1.65	0.16	0.36	12.03
3H-4, 62–63	16.12	3.25	27.1	3.65	0.40	0.07	0.00	6.67
3H-5, 27–28	17.27	4.08	34.0	4.99	0.91	0.12	1.22	8.85
4H-1, 42–43	20.92	4.31	35.9	5.16	0.85	0.12	1.06	8.26
4H-3, 5–6	23.55	4.64	38.7	5.54	0.90	0.12	1.08	8.75
4H-6, 99–100	28.99	5.06	42.1	5.58	0.52	0.09	0.32	6.74
5H-1, 77–78	30.77	4.33	36.1	5.26	0.93	0.13	1.37	8.35
5H-5, 112–113	37.12	4.06	33.8	4.63	0.57	0.10	0.00	6.65
5H-6, 44–45	37.94	5.54	46.1	6.18	0.64	0.09	0.00	8.30
6H-1, 41–42	39.91	3.44	28.7	3.82	0.38	0.09	0.00	4.93
6H-3, 49–50	42.99	2.65	22.1	3.40	0.75	0.12	0.18	7.29
6H-6, 32–33	47.39	3.46	28.8	4.19	0.73	0.12	0.28	7.10
7H-1, 24–25	49.24	3.58	29.8	4.21	0.63	0.10	0.32	7.35
7H-3, 52–53	52.52	3.95	32.9	5.10	1.15	0.13	0.34	10.32
7H-5, 68–69	55.68	3.78	31.5	4.98	1.20	0.13	0.47	10.77
7H-7, 48–49	58.57	3.03	25.2	3.36	0.33	0.07	0.00	5.50
8H-1, 28–29	58.78	3.83	31.9	4.13	0.30	0.07	1.29	5.00
8H-3, 23–24	61.73	6.50	54.1	6.88	0.38	0.09	0.21	4.93
8H-5, 79–80	65.35	5.19	43.2	5.78	0.59	0.10	0.80	6.88
9H-1, 140–141	69.40	5.77	48.1	6.29	0.52	0.09	0.00	6.74
9H-3, 7–8	71.07	3.61	30.1	4.55	0.94	0.14	0.29	7.83
9H-4, 65–66	73.15	3.81	31.7	4.31	0.50	0.09	0.88	6.48
9H-4, 120–121	73.70	4.44	37.0	4.98	0.54	0.09	0.20	7.00
10H-1, 140–141	78.90	5.38	44.8	5.86	0.48	0.09	0.00	6.22
10H-3, 7–8	80.57	6.05	50.4	6.63	0.58	0.09	0.17	7.52
10H-4, 65–66	82.65	3.90	32.5	4.47	0.57	0.08	0.20	8.31
11H-1, 17–18	87.17	5.58	46.5	6.12	0.54	0.09	0.16	7.00
11H-2, 59–60	89.09	4.07	33.9	4.89	0.82	0.08	1.12	11.96
11H-3, 49–50	90.49	4.45	37.1	5.11	0.66	0.12	5.40	6.42
11H-4, 86–87	92.36	3.56	29.7	4.03	0.47	0.08	0.93	6.85
12H-4, 133–134	101.51	6.44	53.6	7.13	0.69	0.07	0.00	11.50
12H-5, 128–129	102.96	4.35	36.2	5.10	0.75	0.09	0.75	9.72
12H-7, 46–47	105.14	5.86	48.8	6.57	0.71	0.10	0.76	8.28
13H-2, 19–20	106.61	4.55	37.9	5.57	1.02	0.12	0.00	9.92
13H-6, 122–123	113.64	4.92	41.0	6.09	1.17	0.13	0.00	10.50
13H-8, 54–55	115.96	4.51	37.6	5.09	0.58	0.09	1.00	7.52
14H-2, 4–5	116.14	5.66	47.1	6.42	0.76	0.09	0.36	9.85
14H-6, 7–8	122.24	5.30	44.1	7.00	1.70	0.10	1.07	19.83
14H-7, 34–35	124.01	2.70	22.5	3.19	0.49	0.11	0.00	5.20
15H-3, 18–19	126.83	2.40	20.0	3.31	0.91	0.11	1.80	9.65
15H-7, 68–69	133.40	3.49	29.1	4.34	0.85	0.12	1.66	8.26
16X-2, 60–61	136.60	3.35	27.9	3.63	0.28	0.09	2.77	3.63
16X-4, 90–91	139.90	3.57	29.7	4.19	0.62	0.10	0.42	7.23
17X-1, 54–55	141.04	4.02	33.5	4.58	0.56	0.11	0.07	5.94
17X-3, 16–17	141.46	4.96	41.3	5.78	0.82	0.19	0.80	5.04
17X-5, 6–7	144.36	3.54	29.5	4.76	1.22	0.10	1.86	14.23
17X-6, 55–56	146.35	3.59	29.9	4.41	0.82	0.12	1.13	7.97
18X-1, 4–5	147.94	3.92	32.7	4.69	0.77	0.09	0.26	9.98
18X-3, 43–44	151.33	3.19	26.6	4.50	1.31	0.16	1.66	9.55
18X-5, 100–101	154.90	3.53	29.4	4.07	0.54	0.10	1.61	6.30
18X-6, 113–114	156.53	5.22	43.5	5.89	0.67	0.10	1.18	7.82
19X-1, 67–68	158.17	1.99	16.6	2.95	0.96	0.11	0.00	10.18
19X-1, 122–123	158.72	3.26	27.2	4.26	1.00	0.15	0.55	7.78
19X-2, 73–74	159.73	3.75	31.2	5.00	1.25	0.14	0.22	10.42
19X-5, 26–28	163.76	3.05	25.4	3.87	0.82	0.09	1.47	10.63
19X-6, 19–20	165.19	4.21	35.1	4.66	0.45	0.09	0.96	5.83
20X-1, 54–55	167.64	3.53	29.4	4.66	1.13	0.13	0.00	10.14
20X-2, 139–140	169.99	3.34	27.8	5.36	2.02	0.15	0.18	15.71
20X-3, 73–74	170.83	3.57	29.7	4.84	1.27	0.13	0.19	11.40
20X-4, 103–104	172.63	2.68	22.3	3.93	1.25	0.11	0.29	13.26
21X-1, 37–38	177.17	3.24	27.0	4.17	0.93	0.10	0.40	10.85
21X-4, 88–89	182.18	4.06	33.8	4.31	0.25	0.14	0.00	2.08
22X-3, 30–31	188.69	3.31	27.6	4.65	1.34	0.14	0.00	11.17
22X-6, 69–70	193.58	3.16	26.3	3.61	0.45	0.10	0.00	5.25
23X-2, 66–67	197.07	3.59	29.9	4.14	0.55	0.11	0.14	5.83
23X-7, 31–32	203.88	5.48	45.6	5.93	0.45	0.08	0.54	6.56
23X-8, 34–35	205.41	5.39	44.9	6.03	0.64	0.10	0.33	7.47
24X-1, 62–63	206.32	3.05	25.4	3.58	0.53	0.11	0.21	5.62
24X-2, 52–53	207.72	0.22	1.8	0.57	0.35	0.04	1.43	10.21
24X-2, 80–81	208.00	2.08	17.3	2.89	0.81	0.19	0.61	4.97
24X-6, 107–108	214.00	5.68	47.3	5.99	0.31	0.08	0.23	4.52
25X-1, 95–96	216.35	3.54	29.5	3.98	0.44	0.10	0.21	5.13
25X-4, 41–42	220.31	3.53	29.4	4.00	0.47	0.10	0.79	5.48
26X-2, 115–116	227.65	2.78	23.2	3.08	0.30	0.09	0.56	3.89
26X-5, 28–29	230.97	4.22	35.2	4.82	0.60	0.11	0.56	6.36
27X-3, 40–41	236.89	2.16	18.0	2.61	0.45	0.09	1.17	5.83
27X-7, 27–28	242.76	3.19	26.6	4.02	0.83	0.13	0.84	7.45
28X-2, 55–56	246.25	4.69	39.1	5.02	0.33	0.09	0.00	4.28
28X-6, 55–56	251.98	4.48	37.3	4.97	0.49	0.11	0.56	5.20
30X-2, 115–116	264.87	4.27	35.6	4.63	0.36	0.09	0.05	4.67
30X-4, 6–7	266.73	2.74	22.8	3.83	1.09	0.14	0.16	9.08

Core, section, interval (cm)	Depth (mbsf)	Inorg. C (wt%)	CaCO <sub>3</sub> (wt%)	TC (wt%)	TOC (wt%)	TN (wt%)	TS (wt%)	C/N
30X-4, 101-102	267.68	2.33	19.4	2.90	0.57	0.17	0.71	3.91
30X-6, 88-89	270.45	2.80	23.3	3.58	0.78	0.12	0.27	7.58
31X-3, 17-18	275.91	4.30	35.8	4.83	0.53	0.10	0.58	6.18
31X-5, 41-42	279.15	2.68	22.3	2.99	0.31	0.09	0.54	4.02
32X-2, 45-46	283.81	3.96	33.0	4.65	0.69	0.12	0.54	6.71
32X-5, 34-35	288.20	4.73	39.4	5.11	0.38	0.09	0.04	4.93
32X-5, 104-105	288.90	8.27	68.9	8.71	0.44	0.03	0.21	17.11
33X-5, 36-37	297.19	4.30	35.8	4.73	0.43	0.09	0.07	5.57
33X-8, 40-41	301.73	3.23	26.9	4.34	1.11	0.14	0.69	9.25
33X-CC, 13-14	301.88	3.32	27.7	4.45	1.13	0.15	0.80	8.79
34X-1, 39-40	302.39	4.17	34.7	4.50	0.33	0.09	0.00	4.28
34X-4, 40-41	306.21	3.69	30.7	4.03	0.34	0.09	0.05	4.41
34X-5, 65-66	307.96	3.61	30.1	4.30	0.69	0.12	0.67	6.71
34X-7, 9-10	310.40	3.34	27.8	3.99	0.65	0.12	0.00	6.32
35X-4, 65-66	316.12	4.25	35.4	4.64	0.39	0.08	0.03	5.69
35X-7, 51-52	320.48	3.36	28.0	4.00	0.64	0.09	0.50	8.30
36X-3, 38-39	324.36	3.57	29.7	3.87	0.30	0.08	0.04	4.38
36X-3, 92-93	324.90	3.21	26.7	3.58	0.37	0.09	0.41	4.80
36X-4, 73-74	326.01	4.01	33.4	4.55	0.54	0.10	0.03	6.30
37X-4, 121-122	335.79	3.37	28.1	3.87	0.50	0.10	0.30	5.83
37X-7, 38-39	339.46	3.21	26.7	3.74	0.53	0.10	0.24	6.18
38X-1, 47-48	340.77	3.45	28.7	3.85	0.40	0.09	0.48	5.19
38X-4, 25-26	344.67	3.03	25.2	3.47	0.44	0.09	0.00	5.70
39X-3, 34-35	353.24	3.01	25.1	3.49	0.48	0.09	0.00	6.22
39X-6, 45-46	357.85	3.43	28.6	4.42	0.99	0.13	0.00	8.88
40X-1, 72-73	360.22	2.96	24.7	3.46	0.50	0.10	0.00	5.83
40X-3, 130-131	363.80	5.15	42.9	5.78	0.63	0.08	0.00	9.19
41X-3, 143-144	373.53	3.88	32.3	4.54	0.66	0.10	0.00	7.70
41X-5, 65-66	375.75	2.99	24.9	4.19	1.20	0.14	0.00	10.00
42X-2, 95-96	379.99	3.79	31.6	4.48	0.69	0.11	0.00	7.32
42X-5, 15-16	383.71	3.60	30.0	4.31	0.71	0.12	0.00	6.90
42X-CC, 11-12	387.95	3.13	26.1	3.70	0.57	0.11	0.00	6.05
43X-6, 30-31	395.61	4.24	35.3	4.79	0.55	0.10	0.00	6.42
44X-1, 25-26	398.35	3.19	26.6	3.82	0.63	0.11	0.00	6.68
44X-6, 44-45	406.04	4.83	40.2	5.36	0.53	0.09	0.00	6.87
45X-1, 115-116	408.85	4.38	36.5	4.87	0.49	0.09	0.00	6.35
45X-1, 117-118	408.87	4.32	36.0	4.26	0.00	0.08	0.00	0.00
46X-6, 47-48	424.76	4.53	37.7	5.09	0.56	0.09	0.00	7.26
46X-7, 116-117	426.95	4.21	35.1	4.74	0.53	0.09	0.00	6.87
47X-2, 99-100	428.72	4.55	37.9	5.16	0.61	0.09	0.00	7.91
48X-1, 103-104	437.63	3.57	29.7	3.93	0.36	0.08	0.00	5.25
48X-2, 46-47	438.56	3.00	25.0	3.85	0.85	0.13	0.00	7.63
48X-2, 74-75	438.84	3.04	25.3	3.82	0.78	0.13	0.00	7.00
48X-2, 104-105	439.14	3.01	25.1	3.85	0.84	0.12	0.00	8.17
48X-5, 80-81	443.40	3.32	27.7	3.76	0.44	0.16	0.00	3.21
49X-2, 49-50	447.44	3.11	25.9	3.73	0.62	0.11	0.00	6.58
49X-3, 58-59	449.03	3.91	32.6	4.24	0.33	0.09	0.00	4.28
49X-6, 103-104	453.98	4.35	36.2	4.70	0.35	0.10	0.00	4.08
50X-1, 34-35	456.14	3.58	29.8	4.15	0.57	0.11	0.00	6.05
50X-6, 16-17	463.46	4.19	34.9	4.75	0.56	0.10	0.00	6.53
51X-3, 67-68	468.51	4.26	35.5	4.71	0.45	0.09	0.00	5.83
51X-5, 32-33	471.10	4.28	35.7	4.93	0.65	0.10	0.00	7.58
51X-CC, 14-15	474.75	3.56	29.7	4.21	0.65	0.09	0.00	8.43
52X-3, 61-62	477.85	3.20	26.7	3.61	0.41	0.09	0.00	5.31
52X-4, 15-16	478.89	3.32	27.7	3.99	0.67	0.11	0.00	7.11
52X-6, 136-137	483.06	3.33	27.7	4.14	0.81	0.12	0.00	7.88
52X-7, 72-73	483.92	3.19	26.6	3.95	0.76	0.12	0.00	7.39
53X-1, 113-114	485.83	3.21	26.7	4.01	0.80	0.10	0.00	9.33
53X-3, 59-60	488.29	3.43	28.6	3.93	0.50	0.10	0.00	5.83
53X-4, 136-137	490.56	3.44	28.7	4.22	0.78	0.11	0.00	8.27
53X-5, 100-102	491.70	3.04	25.3	3.78	0.74	0.10	0.00	8.63
54X-5, 67-69	500.88	3.25	27.1	4.17	0.92	0.10	0.00	10.73
55X-3, 42-43	507.32	3.52	29.3	4.29	0.77	0.10	0.00	8.98
55X-5, 112-113	511.02	4.44	37.0	4.61	0.17	0.10	0.00	1.98
55X-6, 108-109	512.48	3.81	31.7	4.33	0.52	0.08	0.00	7.58
56X-1, 38-39	513.88	3.04	25.3	4.02	0.98	0.12	0.00	9.53
56X-4, 74-75	518.74	4.44	37.0	5.02	0.58	0.08	0.00	8.46
56X-6, 89-90	521.89	3.61	30.1	4.41	0.80	0.10	0.00	9.33
56X-7, 7-8	522.57	3.42	28.5	4.22	0.80	0.10	0.00	9.33
57X-3, 25-26	526.35	4.32	36.0	4.83	0.51	0.07	0.00	8.50
57X-5, 30-31	529.40	3.79	31.6	4.73	0.94	0.12	0.00	9.14
58X-1, 15-16	532.85	4.67	38.9	5.14	0.47	0.08	0.00	6.85
58X-6, 22-24	540.42	4.94	41.2	5.46	0.52	0.07	0.00	8.67
59X-2, 64-65	544.54	3.82	31.8	4.67	0.85	0.11	0.00	9.02
59X-4, 29-30	547.19	3.69	30.7	4.42	0.73	0.10	0.00	8.52
60X-3, 80-81	555.90	3.15	26.2	3.77	0.62	0.10	0.00	7.23
60X-6, 84-85	560.44	3.26	27.2	3.82	0.56	0.10	0.00	6.53
60X-7, 10-11	561.20	3.02	25.2	3.55	0.53	0.10	0.00	6.18
61X-2, 11-12	563.21	3.74	31.2	4.65	0.91	0.11	0.00	9.65
61X-2, 32-33	563.42	3.67	30.6	4.50	0.83	0.10	0.00	9.68
61X-4, 52-53	566.62	4.27	35.6	4.82	0.55	0.07	0.00	9.17
61X-5, 96-97	568.56	6.07	50.6	6.78	0.71	0.09	0.00	9.20
61X-5, 105-106	568.65	4.17	34.7	5.00	0.83	0.10	0.00	9.68
61X-7, 2-3	570.62	2.58	21.5	3.04	0.46	0.09	0.00	5.96
62X-1, 95-96	572.25	4.45	37.1	3.21	0.00	0.10	0.00	0.00
62X-5, 33-34	577.41	4.41	36.7	5.01	0.60	0.07	0.00	10.00
62X-6, 66-67	579.24	4.72	39.3	5.24	0.52	0.08	0.00	7.58

Notes: Total organic carbon (TOC) concentrations are calculated from the difference between inorganic carbon and TC concentrations. C/N ratios are calculated from TOC and total nitrogen (TN) concentrations and are given as atom/atom ratios. TS = total sulfur concentrations. This table is also on the CD-ROM, back pocket, this volume.

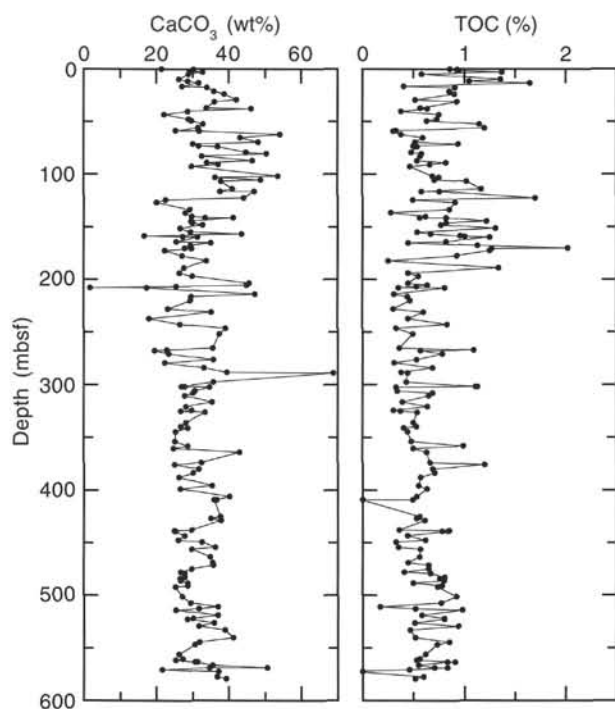


Figure 21. Organic carbon and  $\text{CaCO}_3$  concentrations in sediment samples from Hole 979A.

stratigraphy" section, this chapter). The low background silica concentrations render the interstitial waters highly corrosive to any silica present; hence, a small increase in the siliceous fraction of the sediments will be reflected in the interstitial silica content.

### Conclusions

The interstitial water profiles at Site 979 reflect two main processes, namely organic carbon degradation and the influence of a brine. The effects of organic carbon degradation are to be expected at this site where sediment accumulation rates are high. However, the presence of a brine at depth is unexpected at this location because of the apparent absence of evaporites in this region. The possible presence of brines at Alboran Sea sites during Leg 161 requires further investigation.

## PHYSICAL PROPERTIES

### Introduction

Physical property measurements were made on whole-core sections (for MST and thermal conductivity measurements), split cores (for sonic velocity measurements), and discrete samples (for index properties). Natural gamma ray was measured at 15-cm intervals on cores as part of the MST. Index properties were measured once per alternate section throughout the hole. The gas-charged nature of the recovered cores caused the MST velocity measurements to be unsuccessful. Velocity measurements using DSV and Hamilton Frame transducers were made on every section through Core 979A-9H, at which point the signal strength deteriorated due to the disruption in the cores caused by the gas. The cores from Hole 979A were more disrupted by the effects of gas expansion than those of any other site drilled during Leg 161.

### Multisensor Track

The susceptibility data (Fig. 28A, B) shows periodic variability in the upper 200 m of the hole. Below that depth there is less variability, on wavelengths of 20–40 m or more. The smoothed data (1-m interval; Fig. 28B) is strongly influenced by very high values that were usually found near the top or bottom of the cores. The high values might have been caused by some contaminating material (possibly from the pipe or core barrel) introduced when the cores were compacted within the liners to remove the voids caused by gas expansion at the surface.

The GRAPE density measurements (Fig. 28C) show an increase downhole from  $1.25 \text{ g/cm}^3$  at the surface to  $1.8 \text{ g/cm}^3$  at the bottom of the hole. These measurements also were greatly disrupted by the gas expansion of the cores. There are several changes in the slope of the increase downhole. There is an initial rapid increase to  $1.45 \text{ g/cm}^3$  from 0 to 20 mbsf. The interval from 20 to 250 mbsf shows only a slight increase, with considerable variability on the scale of tens of meters. A steady increase in density is seen from 280 to 420 mbsf, ending at  $1.7 \text{ g/cm}^3$ . The density below that is almost constant until it starts to increase  $\sim 20$  m before the bottom of the hole.

The MST natural gamma sensor data are presented in Figure 28D. There is a nearly constant ratio of thorium to uranium in the sediments, with the total amount increasing only slightly downhole. The abundances may well be constant on a mass basis, with the gradual increase in bulk density downhole. The increase in  $^{40}\text{K}$  downhole is more easily seen and reflects changes in the sediment composition. There are several variations about the general increase that also will need to be compared with the logging results.

### Thermal Conductivity

Thermal conductivity results for Hole 979A are shown in Figure 29 and listed in Table 10 (on CD-ROM, back pocket, this volume). The values at the surface are approximately  $1.2 \text{ W/(m}\cdot\text{K)}$ , in good agreement with the in situ values reported by Polyak et al. (in press). The values increase gradually to about  $1.4 \text{ W/(m}\cdot\text{K)}$  at the bottom of the hole. There are a number of quite low values, below  $1.0 \text{ W/(m}\cdot\text{K)}$ . This is possibly because of the disruption of the core by the high gas content.

### Index Properties

Index property results are presented in Figure 30 and in Table 11 (on CD-ROM, back pocket, this volume). Grain density shows little variation downhole, ranging between  $2.7$  and  $2.8 \text{ g/cm}^3$ . This is consistent with the generally uniform lithology found at this site. Bulk density shows a steady increase from  $1.0 \text{ g/cm}^3$  at the surface to  $1.6 \text{ g/cm}^3$  at the bottom of the hole. There appears to be less scatter in the data and a lower slope to the increase below 500 mbsf. The disruption caused by the gas is shown by several measurements with apparent bulk densities below  $1.0 \text{ g/cm}^3$ . Porosity shows a steady decrease from 65% at the surface to 40% at the bottom of the hole. It also shows a change in slope at 500 mbsf. Void ratio decreases from about 1.6 at 20 mbsf to 0.8 at total depth, again with a change in slope at 500 mbsf.

### P-wave Velocity

DSV and Hamilton frame *P*-wave velocity data are presented in Figure 31 and in Table 12 (on CD-ROM, back pocket, this volume). The limited amount of data generally has values near  $1.52 \text{ km/s}$ , near the velocity of seawater, with only short sections from 12 to 20 mbsf and from 60 to 70 mbsf ranging up to  $1.62 \text{ km/s}$ .

Table 7. Results of Rock-Eval pyrolyses of sapropels selected from Hole 979A.

Core, section, interval (cm)	Depth (mbsf)	TOC (%)	T <sub>max</sub> (°C)	S <sub>1</sub>	S <sub>2</sub>	S <sub>3</sub>	PI	S <sub>2</sub> /S <sub>3</sub>	PC	HI	OI
161-979A-											
1H-1, 9-10	0.09	0.97	461	0.53	6.48	3.18	0.08	2.03	0.58	668	327
2H-2, 10-11	3.10	1.11	412	0.45	5.86	2.73	0.07	2.14	0.52	527	245
3H-2, 50-51	13.00	0.99	415	0.14	2.62	2.77	0.05	0.94	0.23	264	279
4H-3, 5-6	23.55	0.65	431	0.14	1.53	3.02	0.08	0.50	0.13	235	464
7H-5, 68-69	55.68	1.05	412	0.11	2.40	2.57	0.04	0.93	0.20	228	244
9H-3, 7-8	71.07	0.97	422	0.09	2.22	2.08	0.04	1.06	0.19	228	214
13H-2, 19-20	106.61	0.69	524	0.02	1.45	2.17	0.01	0.66	0.12	210	314
17X-5, 6-7	144.36	1.04	423	0.07	3.83	2.32	0.02	1.65	0.32	368	223
19X-2, 73-74	159.73	0.90	416	0.11	3.03	2.30	0.04	1.31	0.26	336	255
20X-3, 73-74	170.83	0.99	423	0.08	3.86	2.50	0.02	1.54	0.32	389	252
24X-2, 80-81	208.00	1.32	395	5.30	3.77	2.33	0.58	1.61	0.75	285	176
30X-4, 6-7	266.73	1.24	414	2.32	3.89	3.18	0.37	1.22	0.51	313	256
33X-8, 40-41	301.73	1.01	423	0.17	3.07	2.06	0.05	1.49	0.27	303	203

Notes: Total organic carbon (TOC) concentrations are derived from the Rock-Eval parameters and therefore differ somewhat from the TOC values of the same samples in Table 6. T<sub>max</sub> values could not be measured accurately for samples with low (<0.5%) TOC contents. Units of the various Rock-Eval parameters are given in the "Explanatory Notes" chapter (this volume).

## DOWNHOLE LOGGING

### Operations

Only Quad combination (quad combo) log data were acquired at Hole 979A. Because of the hole conditions (bridging), logging was performed in two stages and only the quad combo used. After the upper portion of the hole (60–243 mbsf) was logged with the quad combo, we removed the tool from the hole and lowered the pipe to 277 mbsf (1351 mbrf). Logging resumed but several bridges were encountered as the quad combo was lowered into the hole, making it impossible to reach the total depth. The caliper showed that the borehole was washed out (diameter frequently exceeded 18 in) over most of the interval (see "Operations" section, this chapter). Table 13 shows the intervals logged, and the data are shown in Figure 32.

### Results

High gas content in the sediments throughout the hole is suspected to be a major cause for these poor borehole conditions. As observed in previous holes, hole conditions were much better in the upper APC-cored section (80–134 mbsf) than in the interval where XCB was used (134 mbsf to the bottom). Most of the log responses indicate that the entire logged section is rather homogeneous. This was also observed in sedimentological studies, as only one lithologic unit has been recognized in Hole 979A (see "Lithostratigraphy" section, this chapter). Breccia intervals, sands, silts, and diatomaceous deposits are too thin to be individually resolved by the quad combo logs.

Electrical resistivity measurements show a mean value of 0.4–0.5 Ωm, although locally lower values were observed (206, 268, 376, and 385 mbsf). Between 157 and 168 mbsf, intervals with an unusual log response were observed. The resistivity shows a sudden drop (from 0.5 to 0.3 Ωm) at the top of this interval, followed by an increase to 0.8 Ωm at 167 mbsf. Below this depth resistivity drops back to the value typical of the rest of the sequence (0.4–0.5 Ωm; Fig. 33). Acoustic velocity data show a similar pattern, although the velocity data need additional processing to make the pattern clearer. Aboard ship, no obvious reasons were found that might explain these drops in resistivity, and the core descriptions do not identify any lithologic change in this interval. This is not a problem caused by an unusually large borehole diameter, as the caliper shows the borehole is narrower where the resistivity decreases (Fig. 32A). This log response may be related to changing gas amounts or types within the sediments.

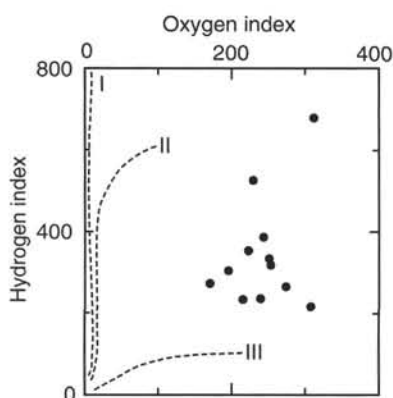


Figure 22. Rock-Eval van Krevelen-type diagram of Pleistocene sapropels from Hole 979A. Organic matter appears to be a mixture of Type II algal material that has been variably oxidized and Type III continental or detrital organic matter. Hydrogen index = mg hydrocarbons/g organic carbon; oxygen index = mg CO<sub>2</sub>/g organic carbon.

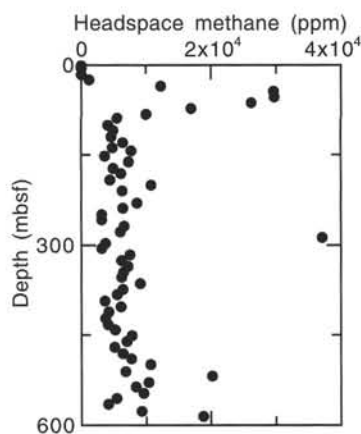


Figure 23. Headspace methane concentrations in sediments from Hole 979A. The decrease in concentrations below 300 mbsf is probably a result of migration of thermogenic methane out of the sediments during the Pliocene.

Table 8. Results of headspace gas analyses of sediments from Hole 979A.

Core, section, interval (cm)	Depth (mbsf)	C <sub>1</sub>	C <sub>2</sub>	C <sub>3</sub>	C <sub>1</sub> /C <sub>2</sub>
161-979A-					
1H-1, 0-5	1	9			
2H-4, 0-5	6	4			
3H-4, 0-5	16	4	2		2
4H-4, 0-5	25	1105			
5H-4, 0-5	35	12280	2		6140
6H-4, 0-5	44	29625	5		5925
7H-4, 0-5	54	29757	6		4960
8H-4, 0-5	63	26193	7		3742
9H-4, 0-5	73	16915	5		3383
10H-4, 0-5	82	9983	4		2496
11H-2, 0-5	89	5472	3		1824
12H-4, 0-5	101	4076			
13H-3, 0-5	109	4868	2		2434
14H-4, 0-5	120	4671	2		2336
15H-4, 0-5	130	6427	3		2142
16X-3, 0-5	138	4836	2		2418
17X-4, 0-5	143	7683	6	3	1281
18X-4, 0-5	152	3605			
19X-4, 0-5	162	7314	3		2438
20X-4, 0-5	172	4932	3		1644
21X-4, 0-5	181	6142	3		2047
22X-4, 0-5	191	4412	3		1471
23X-4, 0-5	200	10778	7	5	1540
24X-4, 0-5	210	6241	3		2080
25X-4, 0-5	230	8559	5	3	1712
26X-3, 0-5	238	6403	3		2134
27X-4, 0-5	249	3119	3	3	1040
28X-4, 0-5	258	3080			
29X-4, 0-5	268	6618	6	7	1103
30X-4, 0-5	278	6042	6	9	1007
31X-4, 0-5	287	37130	17	13	2184
32X-4, 0-5	297	3688	3	4	1229
33X-4, 0-5	306	3117	4	6	779
34X-4, 0-5	316	7470	6	9	1245
35X-4, 0-5	326	6219	6	11	1037
36X-4, 0-5	335	7201	5	7	1440
37X-4, 0-5	345	6467	6	12	1078
38X-4, 0-5	354	6171	7	19	882
39X-4, 0-5	364	9022	7	12	1289
40X-4, 0-5	374	6444	7	15	921
41X-3, 0-5	382	5508	7	20	787
42X-4, 0-5	393	3614	5	15	723
43X-4, 0-5	403	6106	8	23	763
44X-3, 0-5	411	4256	5	13	851
45X-4, 0-5	422	3730	5	21	746
46X-4, 0-5	432	4111	6	25	685
47X-4, 0-5	441	5187	6	23	865
48X-4, 0-5	451	7774	10	49	777
49X-4, 0-5	460	7011	8	29	876
50X-4, 0-5	470	5145	5	16	1029
51X-4, 0-5	480	6421	6	22	1070
52X-4, 0-5	489	7674	14	70	548
53X-4, 0-5	499	10675	10	31	1068
54X-5, 0-5	510	6804	14	61	486
55X-4, 0-5	518	20152	17	43	1185
56X-4, 0-5	528	10370	12	49	864
57X-3, 0-5	536	8391	7	23	1199
58X-4, 0-5	547	9528	16	73	596
59X-3, 0-5	555	5410	10	54	541
60X-3, 0-5	565	4074	6	31	679
61X-4, 0-5	576	9296	14	70	664
62X-4, 0-5	585	18786	24	127	783

Notes: Dominance of methane indicates that most of the gases originate from in situ fermentation of organic matter. The presence of significant amounts of thermogenic propane below 300 mbsf suggests that heat flows were once higher at Site 979.

## IN SITU TEMPERATURE MEASUREMENTS

Three downhole temperature measurements were made with the ADARA temperature tool in Hole 979A. The ADARA temperature data were reduced to in situ values (Table 14). The individual temperature measurement runs are shown in Figure 34. There was a discrepancy in the mud-line temperature between the different runs (Table 14). The same ADARA tool was used for all runs, so the difference, while not currently explained, is not because of differing calibrations. Temperature and thermal conductivity measurement data (see "Physical Properties" section, this chapter) were combined to determine the heat flow. The thermal conductivity shows only a very small trend to

higher conductivity over the depth interval where temperatures were measured. The temperature data were plotted vs. the integrated thermal resistivity in Figure 35. The fit of the temperature points is relatively poor compared to other Leg 161 sites (Fig. 35A). If we use the differences between the reported mud-line temperatures and the equilibrium temperatures, we obtain a much better fit (Fig. 35B). The heat flow at Site 979 is 79 mW/m<sup>2</sup>, using the delta (in situ minus mudline) temperature measurements.

There are eight other heat-flow values in the Southern Alboran Basin (Polyak et al., in press) near Site 979 (Fig. 36). The heat flow found at Site 979 is significantly less than that reported in this area by Polyak et al. (in press). This disagreement with nearby values is the first that was observed on Leg 161. This may be explained by a recent decrease in bottom-water temperature in the Southern Alboran Basin. The heat-flow fit shown in Figure 35A does not intercept the seafloor with the mudline temperature, but rather at mudline + 0.63°C, implying that the current seafloor temperature is that amount below its mean value. If one calculates the heat flow from our shallowest measurement at 20.5 mbsf and its delta temperature of 2.04°C, the result is 111 mW/m<sup>2</sup>, quite close to the 118 ± 8 mW/m<sup>2</sup> reported by Polyak et al. at their measurement closest to Site 979. This close agreement of the heat flow values lends credence to the idea that a bottom-water temperature change may have occurred here, as the equipment used in the previous measurements only measures the temperature gradients in the upper 2 m of the sediments. Their results did indicate approximately linear gradients within that 2-m interval. These combined results will let us put constraints on the time period when the bottom-water temperature change occurred and will show the value of the deeper measurement capability provided by ODP drill holes. The lower value obtained at Site 979, compared to the previous values, may have a significant impact on the tectonic interpretations of this part of the Alboran Basin.

## REFERENCES

- Bouma, A.H., and Brouwer, A. (Eds.), 1964. *Turbidites*. Dev. in Sedimentology, 3: Amsterdam (Elsevier).
- Bourgeois, J., Mauffret, A., Ammar, A., and Demnati, A., 1992. Multichannel seismic data imaging of inversion tectonics of the Alboran Ridge (Western Mediterranean Sea). *Geo-Mar. Lett.*, 12:117-122.
- Chamberlain, C.K., 1978. Recognition of trace fossils in cores. In Basan, P. (Ed.), *Trace Fossil Concepts*. SEPM Short Course, 5:133-183.
- Claypool, G.E., and Kvenvolden, K.A., 1983. Methane and other hydrocarbon gases in marine sediment. *Annu. Rev. Earth Planet. Sci.*, 11:299-327.
- Comas, M.C., García-Dueñas, V., and Jurado, M.J., 1992. Neogene tectonic evolution of the Alboran Basin from MCS data. *Geo-Mar. Lett.*, 12:157-164.
- Comas, M.C., Bourgeois, J., Boulègue, J., Fernandez-Soler, J.M., de la Linde, J., and Soto, J.L., in press. Preliminary results of the Cyanalboran cruise: dives of the submersible CYANA in the Alboran Sea. *Terra Nova*.
- de Larouzière, F.D., Bolze, J., Bordet, P., Hernandez, J., Montecat, C., and Ott d'Estevou, P., 1988. The Betic segment of the lithospheric trans-Alboran shear zone during the Late Miocene. *Tectonophysics*, 152:41-52.
- Emerson, S., and Hedges, J.L., 1988. Processes controlling the organic carbon content of open ocean sediments. *Paleoceanography*, 3:621-634.
- Espitalié, J., Laporte, J.L., Leplat, P., Madec, M., Marquis, F., Paulet, J., and Boutefeu, A., 1977. Méthode rapide de caractérisation des roches mères, de leur potentiel pétrolier et de leur degré d'évolution. *Rev. Inst. Fr. Pet.*, 32:23-42.
- Giermann, G., Pfannenstiel, M., and Wimmenauer, W., 1968. Relation entre morphologie, tectonique et volcanisme en mer d'Alboran (Méditerranée occidentale): résultats préliminaires de la campagne Jean-Charcot (1967). *C. R. Somm. Seances Soc. Geol. Fr.*, 4:116-118.
- Hernandez, J., de Larouzière, F.D., Bolze, J., and Bordet, P., 1987. Le magmatisme néogène bético-rifain et le couloir de décrochement trans-Alboran. *Bull. Soc. Geol. Fr.*, 3:257-267.
- Manheim, F.T., and Sayles, F.L., 1974. Composition and origin of interstitial waters of marine sediments, based on deep sea drill cores. In Goldberg,

- E.D. (Ed.), *The Sea* (Vol. 5): *Marine Chemistry: The Sedimentary Cycle*. New York (Wiley), 527–568.
- Mauffret, A., El-Robrini, M., and Gennesseaux, M., 1987. Indice de la compression récente en mer Méditerranée: un bassin losangique sur la marge nord-algérienne. *Bull. Soc. Geol. Fr.*, 8:1195–1206.
- Mauffret, A., Maldonado, A., and Campillo, A.C., 1992. Tectonic framework of the Eastern Alboran and Western Algerian Basins, Western Mediterranean. *Geo-Mar. Lett.*, 12:104–110.
- McIver, R.D., 1975. Hydrocarbon occurrences from JOIDES Deep Sea Drilling Project. *Proc. Ninth Petrol. Congr.*, 269–280.
- Meyers, P.A., 1994. Preservation of elemental and isotopic source identification of sedimentary organic matter. *Chem. Geol.*, 144:289–302.
- Meyers, P.A., and Brassell, S.C., 1985. Biogenic gases in sediments deposited since Miocene times on the Walvis Ridge, South Atlantic Ocean. In Caldwell, D.E., Brierley, J.A., and Brierley, C.L. (Eds.), *Planetary Ecology*: New York (Van Nostrand Reinhold), 69–80.
- Meyers, P.A., and Shaw, T.J., 1996. Organic matter accumulation, sulfate reduction, and methanogenesis in Pliocene-Pleistocene turbidites on the Iberia Abyssal Plain. In Whitmarsh, R.B., Sawyer, D.S., Klaus, A., and Masson, D.G. (Eds.), *Proc. ODP, Sci. Results*, 149: College Station, TX (Ocean Drilling Program), 705–712.
- Meyers, P.A., and Snowdon, L.R., 1993. Sources and migration of methane-rich gas in sedimentary rocks on the Exmouth Plateau: northwest Australian continental margin. In Oremland, R.S. (Ed.), *Biogeochemistry of Global Change*: New York (Chapman and Hall), 434–446.
- Pickering, K.T., Hiscott, R., and Hein, F.J., 1989. *Deep-Marine Environments: Clastic Sedimentation and Tectonics*: London (Unwin Hyman).
- Polyak, B.G., Fernández, M., Khutorsky, M.D., Soto, J.I., Basov, I.A., Comas, M.C., Kain, V.Ye., Alonso, B., Apagova, G.V., Mazurova, I.S., Negrodo, A., Tochitsky, V.O., de la Linde, J., Bogdanov, N.A., and Banda, E., in press. Heat flow in the Alboran Sea (the Western Mediterranean). *Tectonophysics*.
- Shipboard Scientific Party, 1990. Site 767. In Rangin, C., Silver, E.A., von Breyman, M.T., et al., *Proc. ODP, Init. Repts.*, 124: College Station, TX (Ocean Drilling Program), 121–193.
- Watts, A.B., Platt, J.P., and Bulh, P., 1993. Tectonic evolution of the Alboran Sea Basin. *Basin Res.*, 5:153–177.
- Woodside, J.M., and Maldonado, A., 1992. Styles of compressional neotectonics in the Eastern Alboran Sea. *Geo-Mar. Lett.*, 12:111–116.
- Wright, R., 1978. Neogene paleobathymetry of the Mediterranean based on benthic foraminifers from DSDP Leg 42. In Hsü, K.J., Montadert, L., et al., *Init. Repts. DSDP*, 42 (Pt. 1): Washington (U.S. Govt. Printing Office), 837–846.

Ms 16IIR-109

**NOTE: For all sites drilled, core-description forms (“barrel sheets”) and core photographs can be found in Section 3, beginning on page 429. Smear-slide data can be found in Section 4, beginning on page 949. Thin-section data can be found in Section 5, beginning on page 991. See Table of Contents for material contained on CD-ROM.**

Table 9. Interstitial water data from Hole 979A.

Core, section, interval (cm)	Depth (mbsf)	pH	Alkalinity (mM)	Salinity (‰)	Cl (mM)	Ca (mM)	Mg (mM)	Mn (μM)	Sr (μM)	SO <sub>4</sub> (mM)	NH <sub>4</sub> (mM)	H <sub>4</sub> SiO <sub>4</sub> (μM)	Li (μM)	Na (mM)	K (mM)	PO <sub>4</sub> (μM)
161-979A-																
2H-3, 145–150	5.95	7.65	6.425	38	632	10.77	59.79	8.5	86	27.1	0.69	866	30	557	12.98	33.4
3H-3, 145–150	15.45	7.63	15.414	37.5	626	6.07	54.02	4.0	77	15.2	1.41	713	36	544	11.72	30.0
4H-3, 145–150	24.95	7.53	16.81	38	640	3.49	44.94	3.0	107	0.5	2.76	784	35	548	11.68	77.3
5H-3, 145–150	34.45	7.57	13.5	38	650	5.12	46.05	3.5	151	0.0	3.06	596	41	564	11.20	17.9
6H-3, 145–150	43.95	7.50	11.882	38	687	5.08	45.69	6.0	182	0.7	3.48	765	46	567	12.45	25.4
9H-3, 145–150	72.45	7.15	8.422	42	759	9.37	47.64	3.0	289	0.8	4.92	832	90	611	12.72	20.2
12H-3, 145–150	100.13	7.05	8.311	46	834	10.97	57.76	4.5	398	0.7	6.55	503	129	659	12.23	n.d.
15H-3, 145–150	128.10	7.32	8.198	50.5	915	16.10	64.48	9.5	605	1.9	8.29	821	178	707	13.08	22.5
18X-3, 145–150	152.35	6.81	6.556	53.5	957	21.81	68.04	5.0	612	1.0	8.63	1037	226	772	11.39	16.7
21X-3, 145–150	181.25	6.78	5.397	56	997	25.94	72.12	5.5	670	1.4	9.80	678	308	794	11.30	28.3
24X-3, 140–150	210.10	6.80	4.927	62	1088	33.73	77.07	13.5	964	0.5	9.82	747	424	865	11.71	21.9
27X-3, 140–150	237.89	7.05	4.52	64	1130	41.39	79.39	10.5	1168	0.0	9.67	646	511	905	10.42	20.2
30X-3, 135–145	266.57	7.08	3.926	70	1204	45.83	76.14	8.0	1191	0.4	11.69	966	630	939	11.67	24.2
33X-3, 140–150	295.78	6.91	2.501	70	1244	47.19	80.86	9.5	1410	0.7	11.11	304	668	979	9.97	21.9
36X-3, 120–130	325.18	6.70	2.693	72	1286	54.28	81.04	7.5	1626	0.8	10.83	520	768	1019	9.61	9.2
39X-3, 140–150	354.30	7.02	3.676	76	1348	62.22	78.94	11.5	1735	0.6	11.34	527	922	1039	9.40	34.0
42X-3, 140–150	381.96	6.59	4.174	78	1384	68.69	78.62	15.0	1955	0.5	11.70	572	1018	1105	9.26	18.5
45X-3, 140–150	412.10	6.87	1.567	80	1412	68.38	74.53	8.5	2120	0.9	10.83	187	1040	1113	9.77	7.6
48X-3, 140–150	441.00	6.48	1.561	84	1478	78.33	72.75	11.0	2520	0.0	11.13	481	1082	1155	7.43	5.4
51X-3, 140–150	469.24	6.68	1.758	86	1504	79.75	70.05	7.5	2605	0.7	12.21	205	1124	1185	8.73	4.9
54X-4, 140–150	500.11	6.84	1.626	88	1584	86.83	69.29	9.5	2863	0.1	13.27	367	1176	1261	8.25	9.2
57X-2, 135–150	525.95	6.56	1.626	91	1620	90.04	67.85	9.5	2968	0.4	13.12	438	1062	1249	7.84	n.d.
60X-2, 135–150	554.95	7.17	1.429	95	1654	90.98	67.12	8.0	3297	0.2	13.30	86	954	1320	6.69	n.d.

Note: n.d. = not determined. This table is also on the CD-ROM, back pocket, this volume.

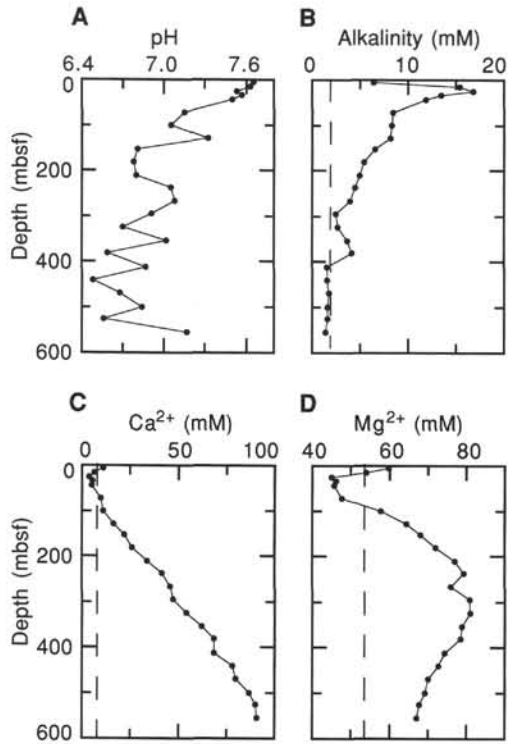


Figure 24. Concentration profiles of (A) pH, (B) alkalinity, (C) calcium, and (D) magnesium in Hole 979A. The dashed lines indicate standard seawater (International Association for the Physical Sciences of the Ocean [IAPSO]) composition.

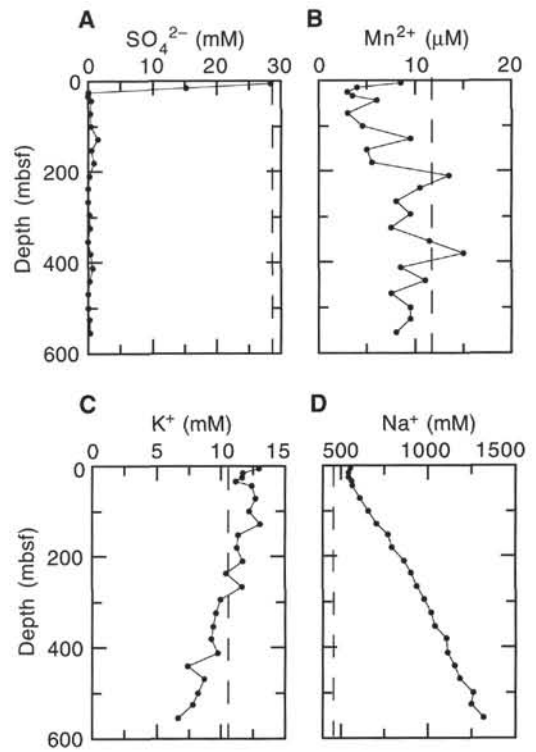


Figure 26. Concentration profiles of (A) sulfate, (B) manganese, (C) potassium, and (D) sodium in Hole 979A. The dashed lines indicate standard seawater (IAPSO) composition.

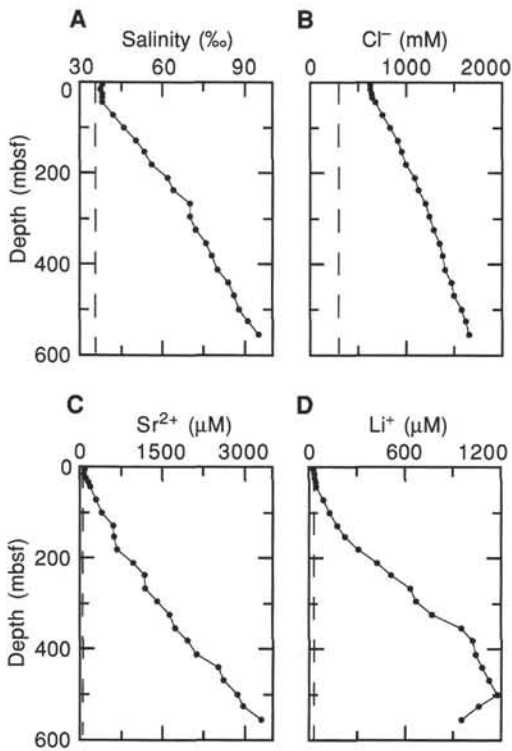


Figure 25. Concentration profiles of (A) salinity, (B) chloride, (C) strontium, and (D) lithium in Hole 979A. The dashed lines indicate standard seawater (IAPSO) composition.

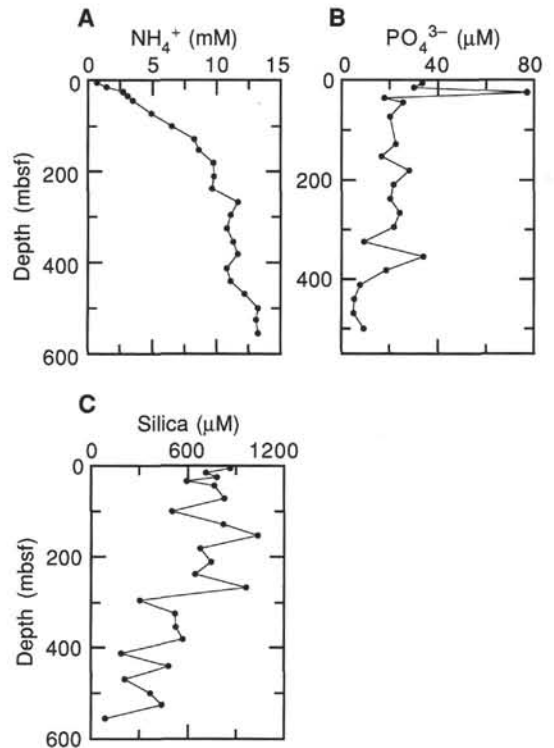


Figure 27. Concentration profiles of (A) ammonium, (B) phosphate, and (C) silica in Hole 979A.

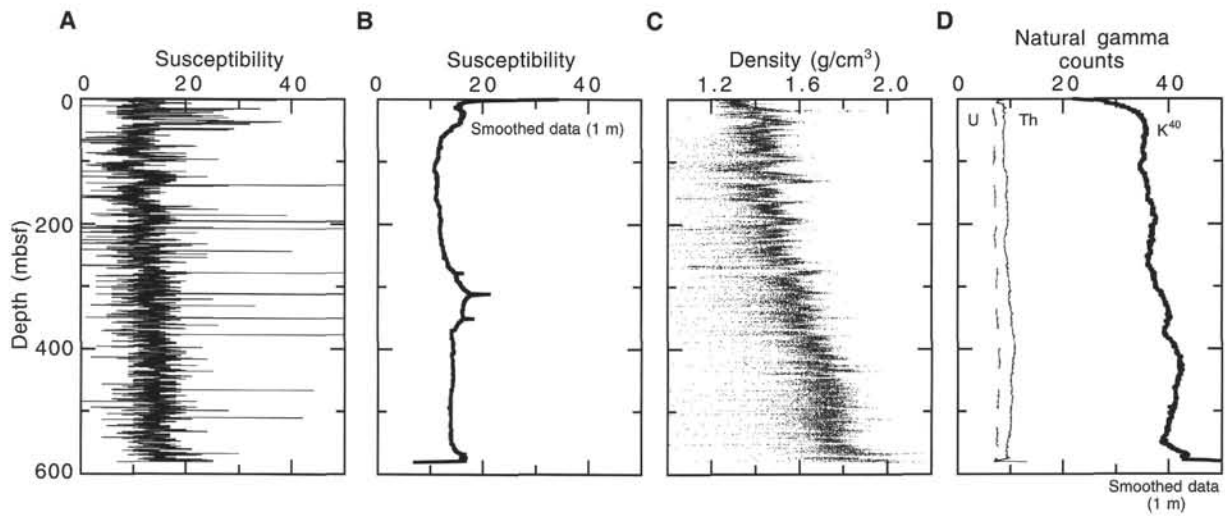


Figure 28. MST data for Hole 979A: (A) susceptibility, (B) 1-m smoothed susceptibility, (C) density, and (D) 1-m smoothed uranium, thorium, and <sup>40</sup>K from natural gamma.

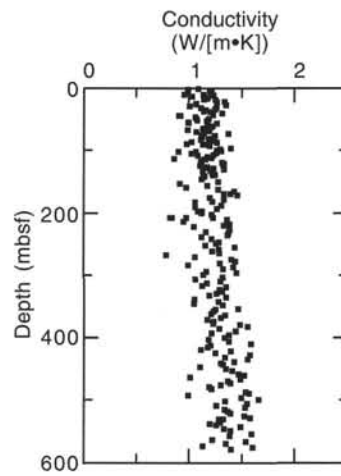


Figure 29. Thermal conductivity data for Hole 979A.

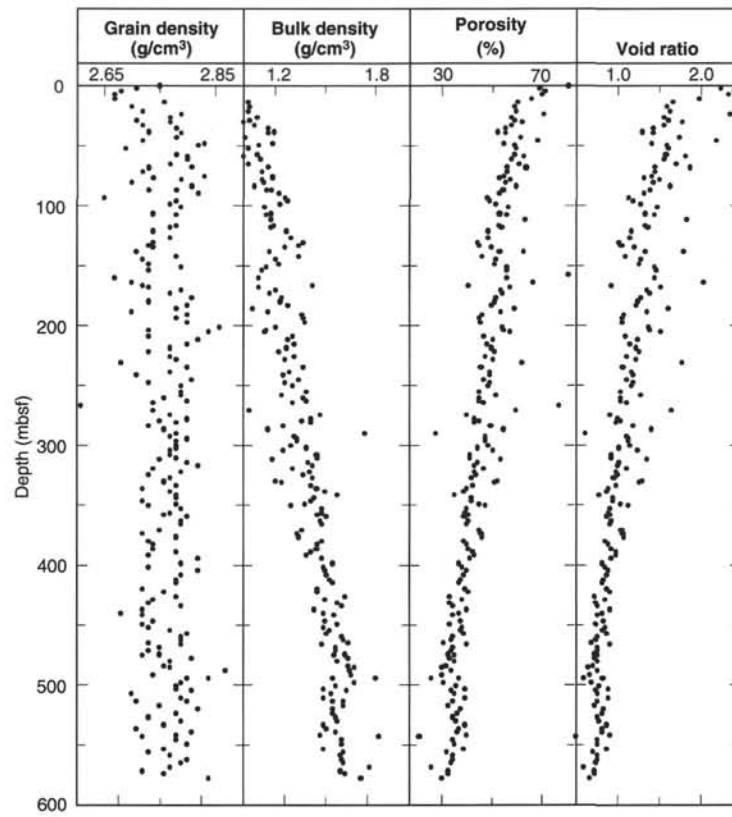


Figure 30. Index property data for Hole 979A.

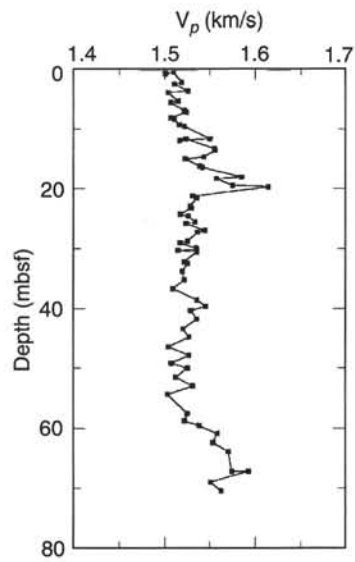


Figure 31. Seismic velocity data for Hole 979A.

Table 13. Logged depth intervals in Hole 979A.

String	Run	Depth		Tools
		(mbsf)	(mbrf)	
Quad combo	Up 1	243.0-60.0	1317.0-1134.0	NGT/SDT/CNT-G/HLDT/DIT-E/TLT
	Up 2	456.0-249.0	1530.0-1323.0	NGT/SDT/CNT-G/HLDT/DIT-E/TLT
	Up 3*	316.0-249.0	1390.0-1323.0	NGT/SDT/CNT-G/HLDT/DIT-E/TLT

Notes: \* = repeat section. Note: mbsf = meters below seafloor, mbrf = meters below rig floor.

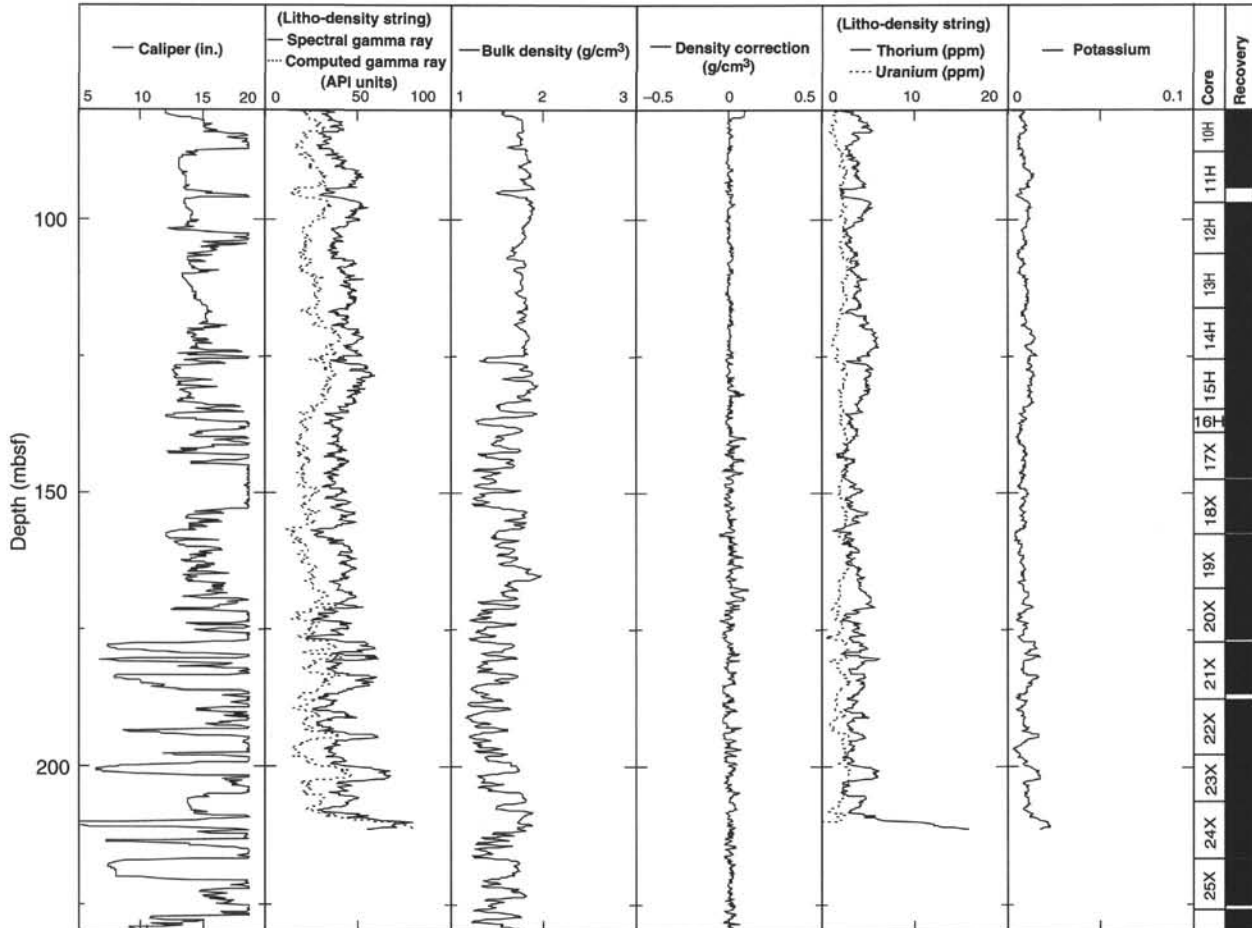


Figure 32. Quad combo results for Hole 979A.

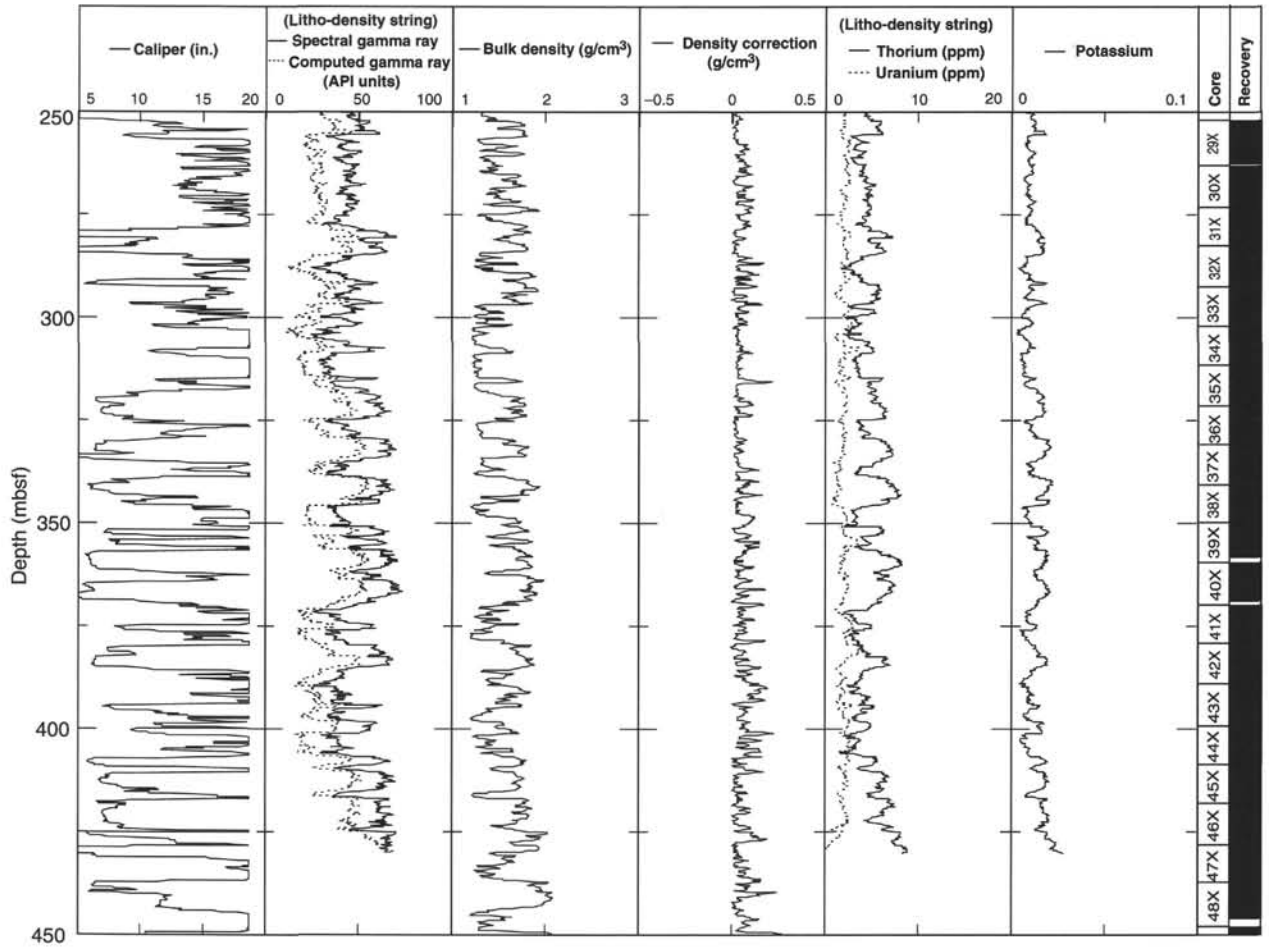


Figure 32 (continued).

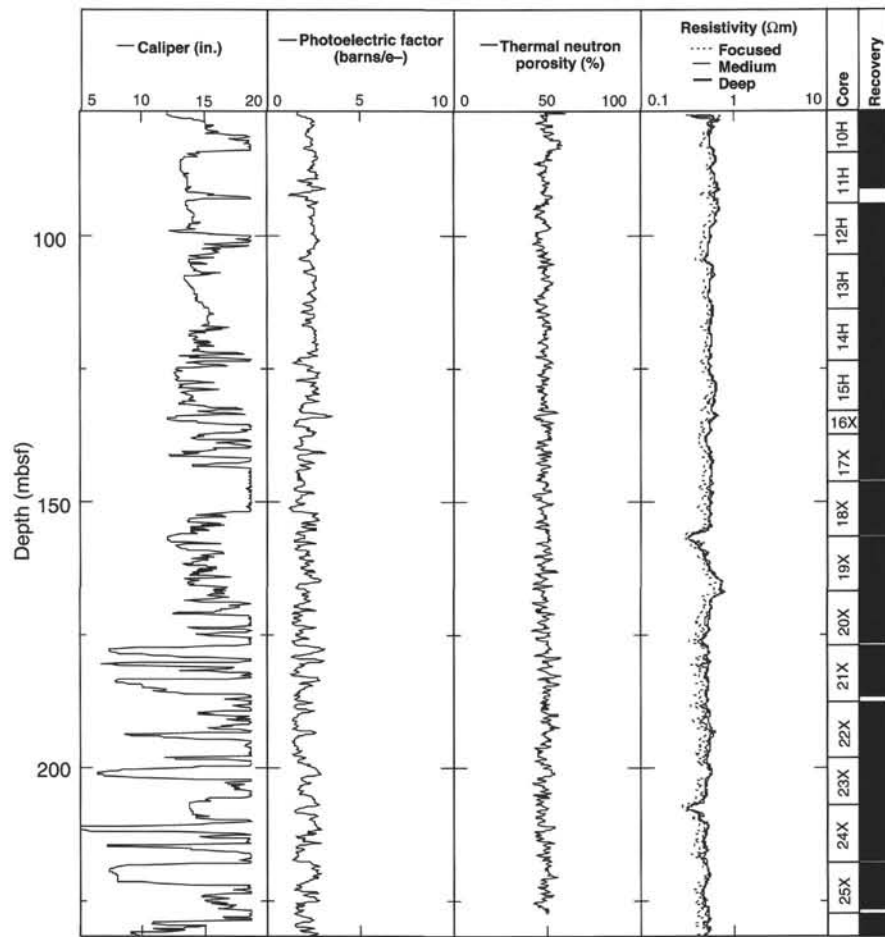


Figure 32 (continued).

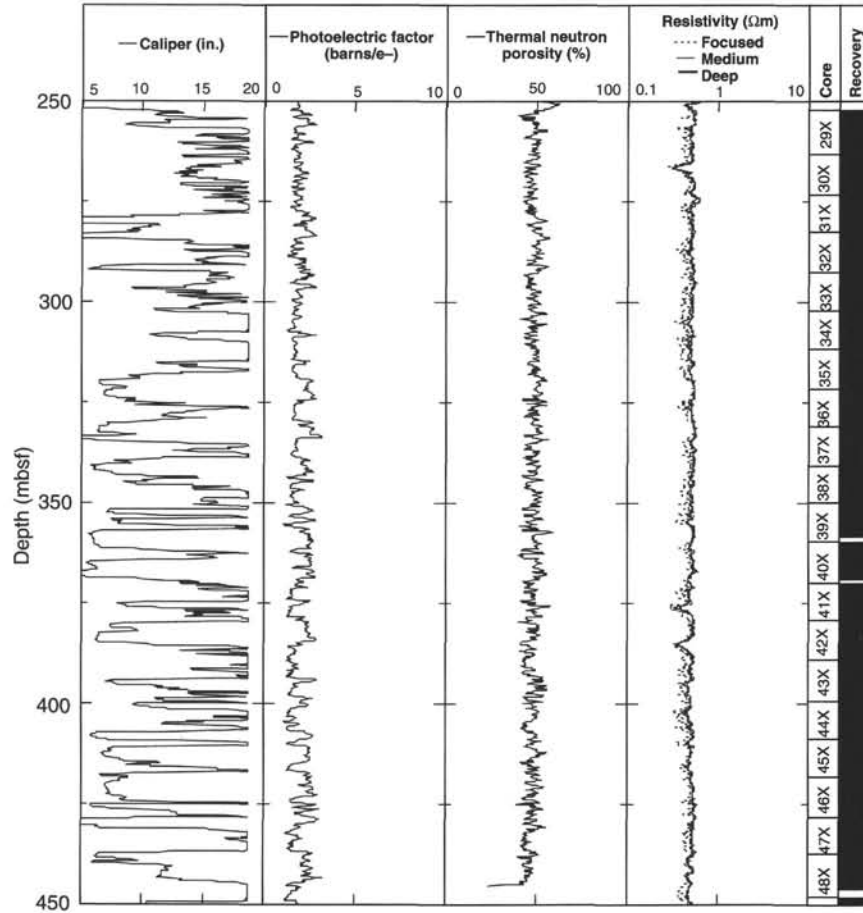


Figure 32 (continued).

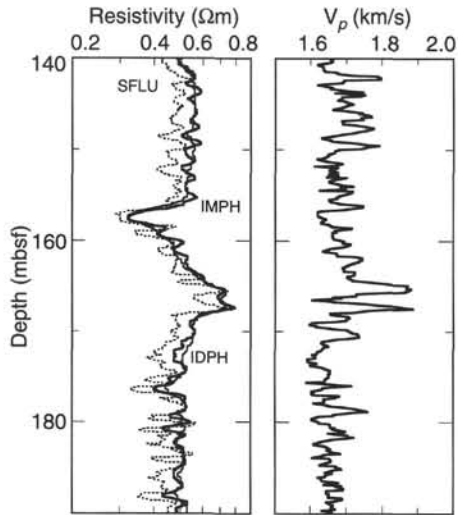


Figure 33. Resistivity and velocity anomaly in the upper logged section in Hole 979A.

Table 14. ADARA temperature measurements and computed temperature parameters at Hole 979A.

Depth (mbsf)	Temperature (°C)	Mud-line temperature (°C)	Δ Temperature (°C)	I.T.R. (k·m <sup>2</sup> )/W
20.5	11.406	9.366 ± 0.008	2.040	18.344
49.0	14.233	10.165 ± 0.017	4.068	43.013
77.5	16.075	10.124 ± 0.024	5.951	68.033

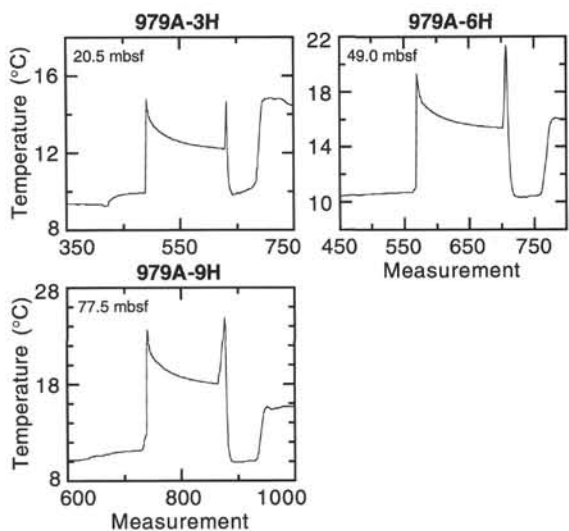


Figure 34. Temperature vs. time for the individual ADARA temperature tool runs at Hole 979A.

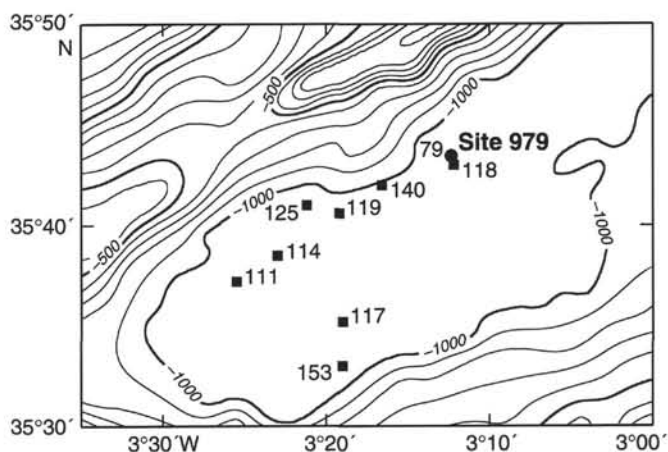


Figure 36. Heat flow measurements with values in  $mW/m^2$  in the vicinity of Site 979 (shown by the solid circle). Data, shown by squares, are from Polyak et al. (in press). Bathymetric contours at 100-m intervals.

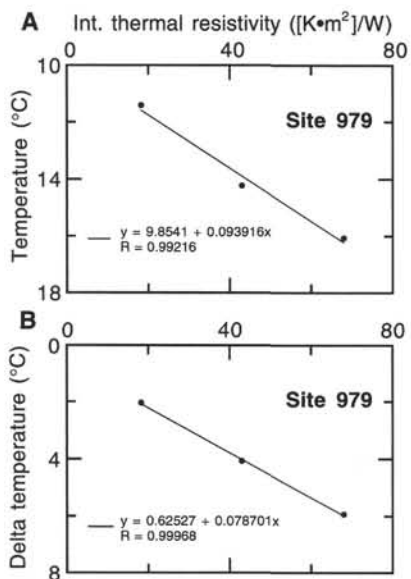


Figure 35. Temperature vs. integrated thermal resistivity for Hole 979A. **A.** Reported temperatures. **B.** Delta temperatures (reported minus mud line).

## SHORE-BASED LOG PROCESSING

## Hole 979A

**Bottom felt:** 1074 mbrf (used for depth shift to seafloor)

**Total penetration:** 580.9 mbsf

**Total core recovered:** 583.1 m (100.4%)

### Logging Runs

**Logging string 1:** DIT/SDT/HLDT/CNTG/NGT (upper and lower sections)

Wireline heave compensator was used to counter ship heave.

### Bottom-Hole Assembly

The following bottom-hole depth assembly are as they appear on the logs after differential depth shift (see "Depth shift" section) and depth shift to the seafloor. As such, there might be a discrepancy with the original depths given by the drillers onboard. Possible reasons for depth discrepancies are ship heave, use of wireline heave compensator, and drill string and/or wireline stretch.

DIT/SDT/HLDT/CNTG/NGT: Bottom-hole assembly at ~80 mbsf (upper section).

DIT/SDT/HLDT/CNTG/NGT: Bottom-hole assembly at ~237 mbsf (lower section).

### Processing

**Depth shift:** Only one logging string run; no differential depth shift required. All original logs have been depth shifted to the seafloor (-1074 m).

**Gamma-ray processing:** NGT data have been processed to correct for borehole size and type of drilling fluid.

**Acoustic data processing:** The array sonic tool was operated in two modes: linear array mode, with the 8 receivers providing full waveform analysis (compressional and shear) and standard depth-derived borehole compensated mode, including long-spacing (8-10-10-12 ft) and short-spacing (3-5-5-7 ft) logs. At Hole 979A the acoustic data were greatly affected by the large and irregular borehole; because of the lack of a good set of transit times the routine processing could not be performed. Therefore, velocity has been estimated by the best single channel, not borehole-compensated, reading.

### Quality Control

Data recorded through bottom-hole assembly, such as the gamma ray and neutron porosity data above 80 and 237 mbsf, should be used qualitatively only because of the attenuation on the incoming signal. Invalid data were recorded on the gamma ray log at 64, 72-76, and 243-248 mbsf.

Hole diameter was recorded by the hydraulic caliper on the HLDT tool (CALI).

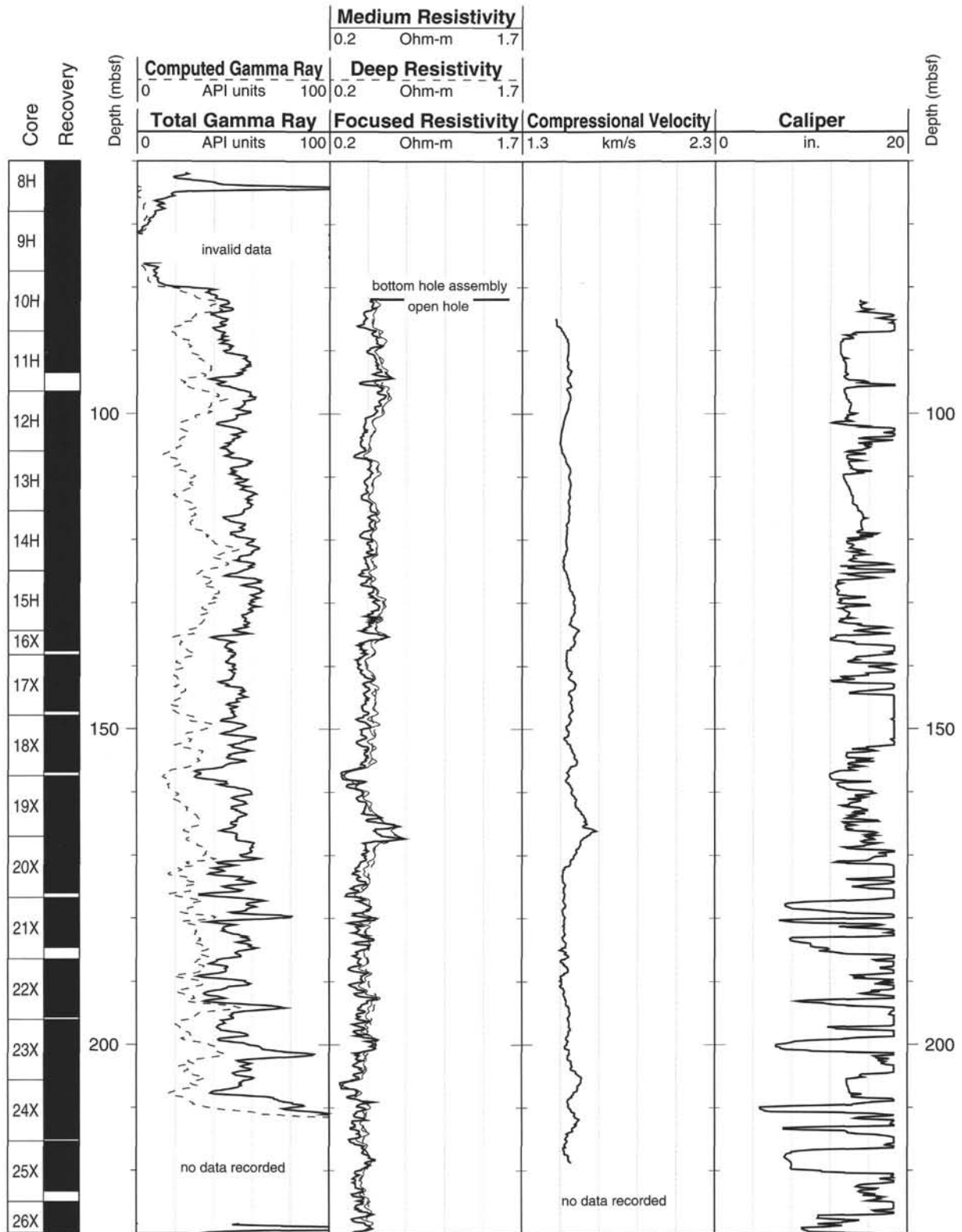
**Note:** Details of standard shore-based processing procedures are found in the "Explanatory Notes" chapter, this volume. For further information about the logs, please contact:

Cristina Broglia  
Phone: 914-365-8343  
Fax: 914-365-3182

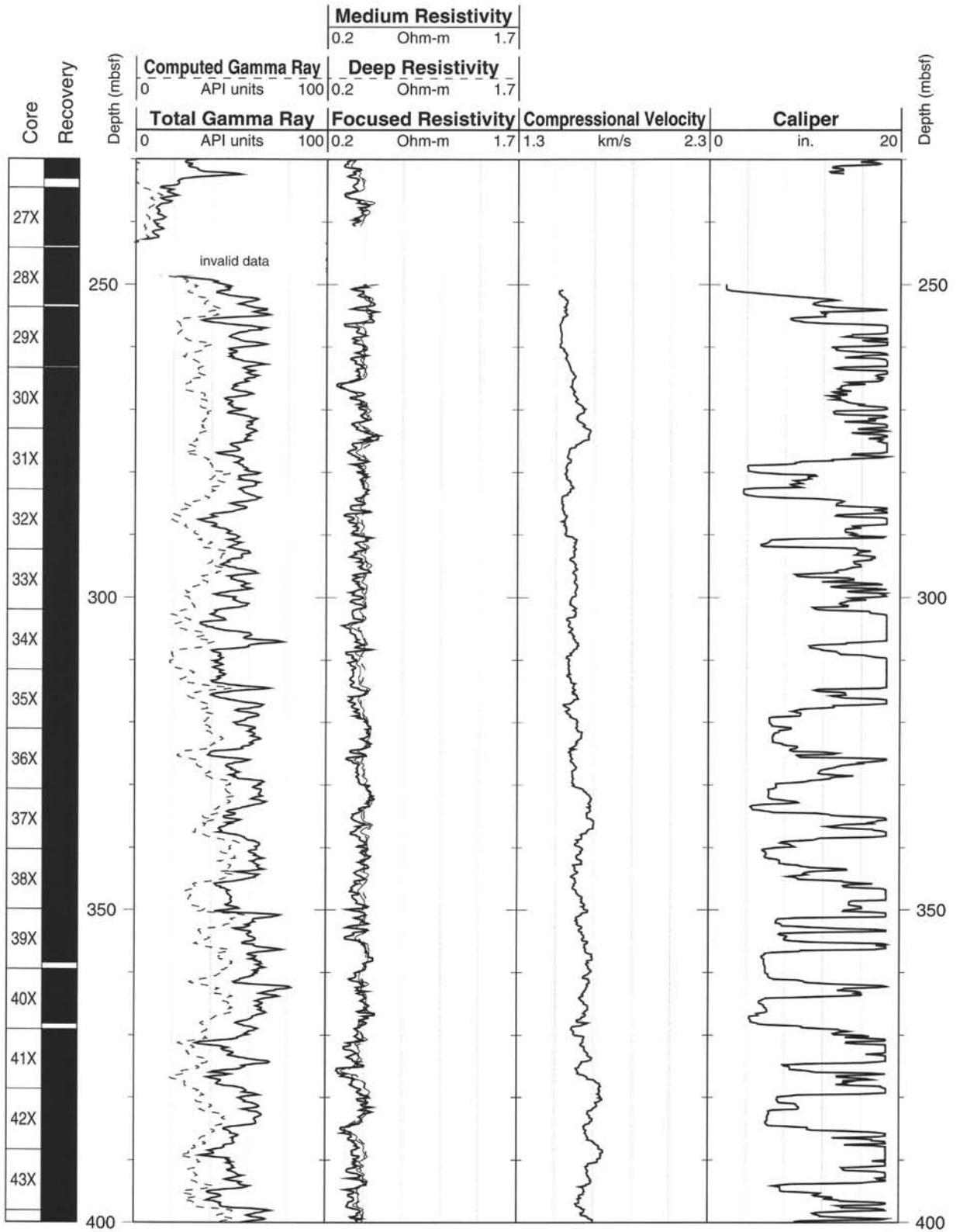
E-mail: [chris@ldeo.columbia.edu](mailto:chris@ldeo.columbia.edu)

Elizabeth Pratson  
Phone: 914-365-8313  
Fax: 914-365-3182  
E-mail: [beth@ldeo.columbia.edu](mailto:beth@ldeo.columbia.edu)

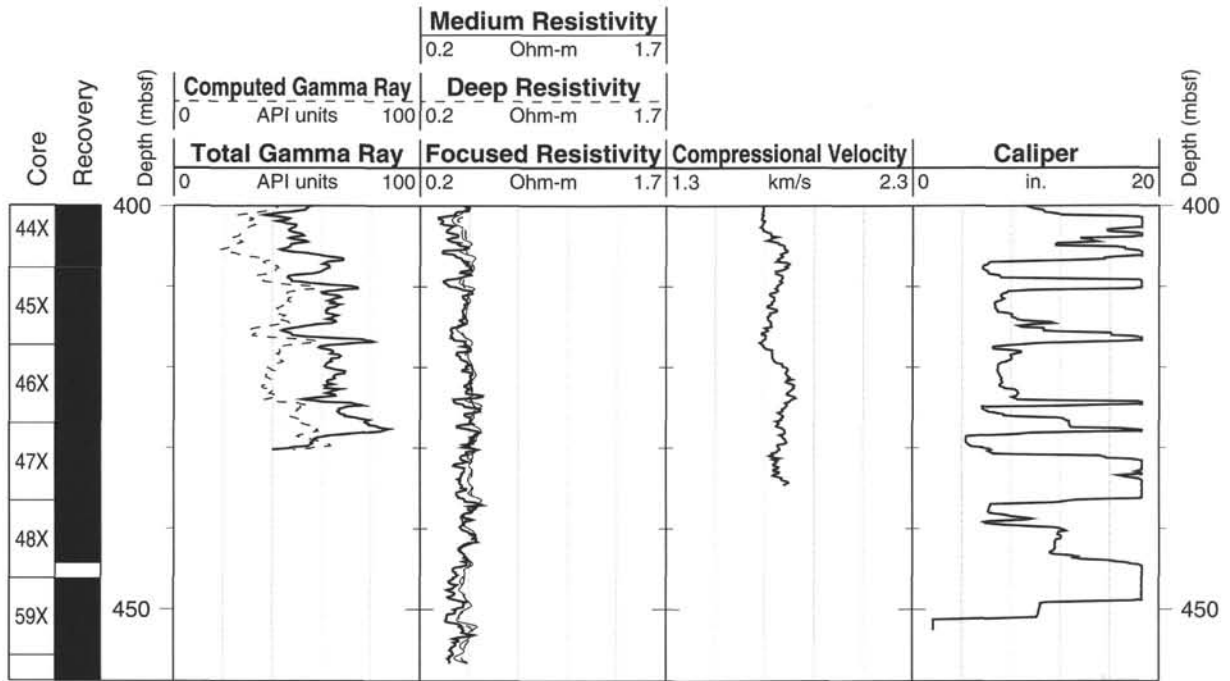
Hole 979A: Natural Gamma Ray-Resistivity-Sonic Logging Data



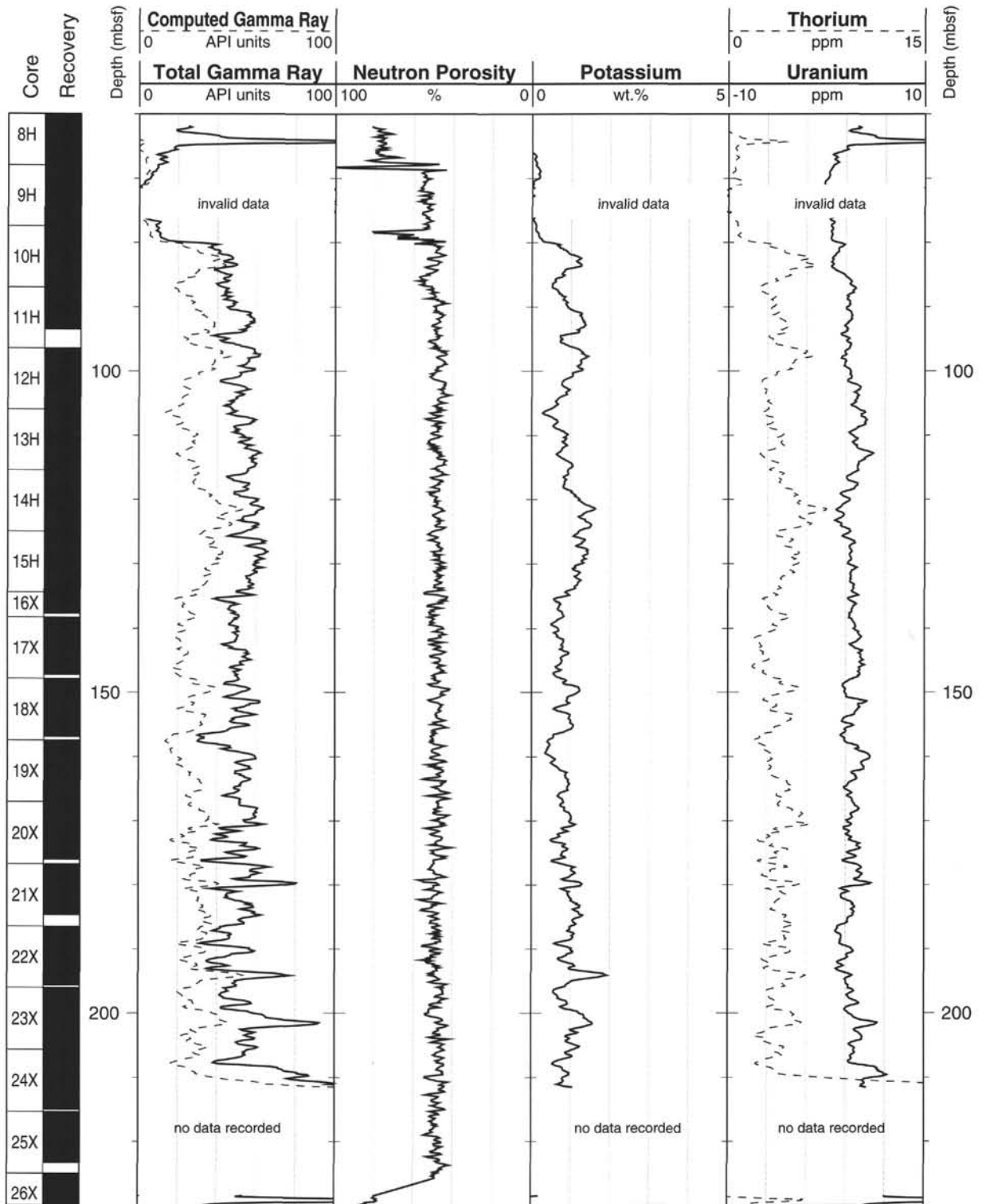
Hole 979A: Natural Gamma Ray-Resistivity-Sonic Logging Data (cont.)



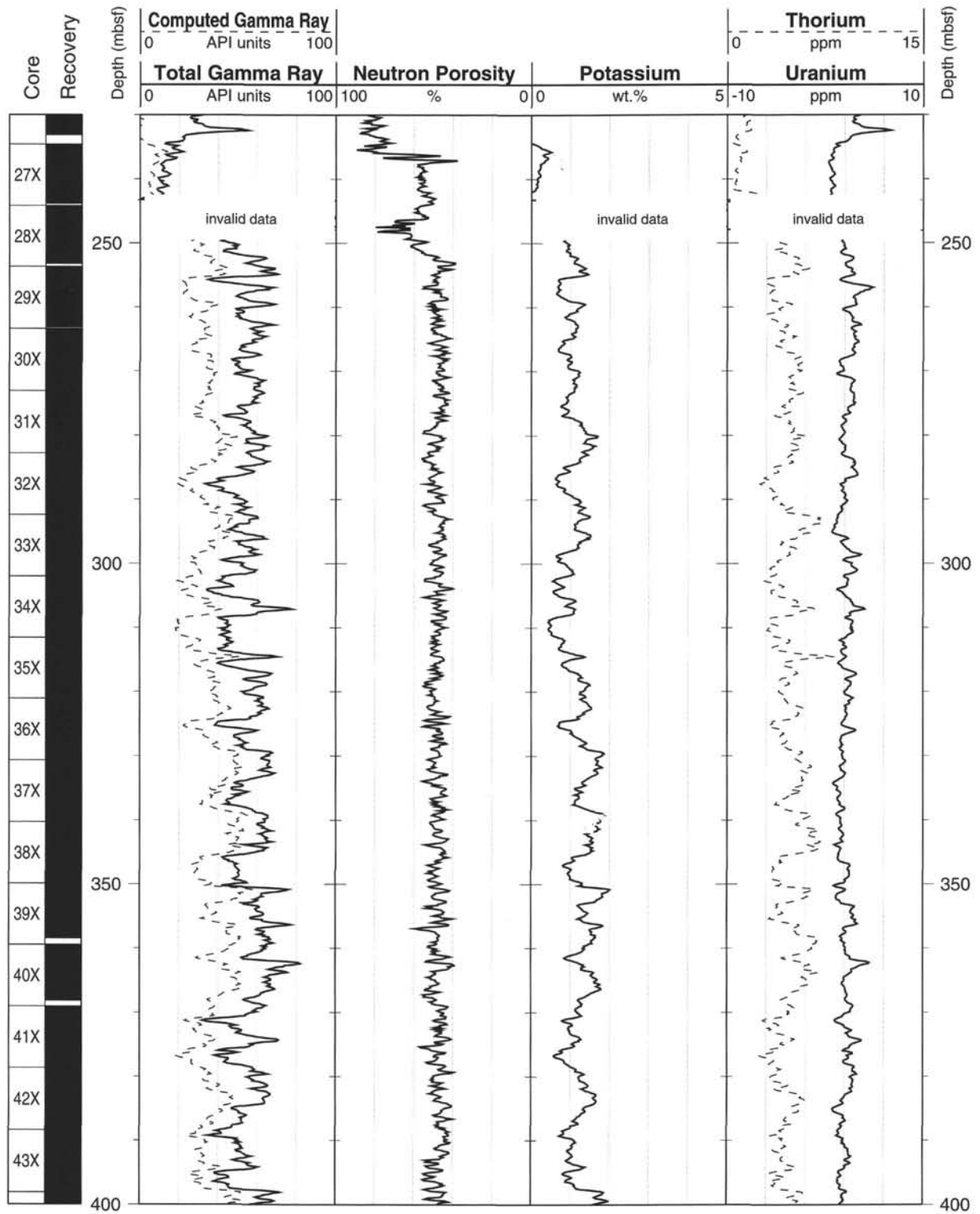
Hole 979A: Natural Gamma Ray-Resistivity-Sonic Logging Data (cont.)



Hole 979A: Natural Gamma Ray-Porosity Logging Data



Hole 979A: Natural Gamma Ray-Porosity Logging Data (cont.)



Hole 979A: Natural Gamma Ray-Porosity Logging Data (cont.)

